Topaz-bearing Lower Ordovician orthogneiss within the Ostrong Nappe System – The Laimbach Orthogneiss (Bohemian Massif, Lower Austria)

Annika Geringer[1*], Christoph Iglseder[1], Urs Klötzli[2], Bernhard Grasemann[3], Jiří Sláma[4]

[1] GeoSphere Austria, Hohe Warte 38, 1190 Wien, Austria;

[2] Department of Lithospheric Research, University of Vienna, Josef-Holaubek-Platz 2, 1090 Wien, Austria;

[3] Department of Geology, University of Vienna, Josef-Holaubek-Platz 2, 1090 Wien, Austria;

[4] Institute of Geology, Czech Academy of Sciences, Rozvojová 269, Prague 6 16500, Czech Republic;

[*] Corresponding author: annika.geringer@geosphere.at

Abstract

In the 1980s, large parts of the Bohemian Massif in Austria were explored for the occurrence of raw materials (Göd, 1988), and a trace content of topaz was discovered in channels draining the eastern slope of the Ostrong (Lower Austria). Orthogneiss bodies in the Ostrong Nappe System are shown to be the source of these topaz occurrences, and Raman spectroscopy indicates that topaz is fluorine rich. So far, this is the only occurrence of topaz-bearing orthogneiss within the entire Moldanubian Superunit. The orthogneiss shows a tectonic overprint and exhibits a weak to well-developed foliation, as well as local folding. Samples taken near the tectonic boundary of the Ostrong to the Drosendorf Nappe Systems show stronger shear deformation with a pronounced mylonitic foliation and stretching lineation. Detailed geochemical investigations of the major and trace elements indicate a classification as S-type granite with a high degree of differentiation and a peraluminous character. The orthogneiss has a high SiO_2 content of 72.8–77.3 wt%, as well as a noteworthy high fluorine content of up to 2760 ppm. Mineral compositions show zoned plagioclase with an albite component of about 87–99 mol%, increasing towards the grain margin. Garnet occurs rarely, but consistently in those samples near the tectonic boundary of the Ostrong- to the Drosendorf Nappe Systems. Garnet is almandine-dominated, shows no zoning and is single-phased. Sillimanite is common and samples near the tectonic boundary also contain kyanite. To determine the previously unknown protolith age of the orthogneiss, U-Pb zircon dating was applied. Three zircon fractions from two samples yield concordia ages of 475.3 ± 1.0 Ma, 474.8 ± 2.9 Ma, and 473.5 ± 1.5 Ma, identical in assigned uncertainties, reflecting magmatic zircon growth. Furthermore, the short prismatic habit of zircon grains indicates a plutonic rather than volcanic origin of the protolith. Dating results also provide a minimum sedimentation age for the rocks of the Ostrong Nappe System within Austria. In comparison with other metagranitoids and orthogneisses of the Moldanubian Nappes, the investigated orthogneiss shows strong similarities with the Gföhl Gneiss and the Moldanubian Granulite. The orthogneiss therefore is considered as a more fractionated equivalent of the Gföhl Gneiss. In conclusion we suggest to name the studied orthogneiss *Laimbach Orthogneiss* in the rank of a lithodeme (NACSN, 2005), after the locality Laimbach am Ostrong (48°19′01″N; 15°07′19″E), which is located centrally with respect to the occurrences of this gneiss.

1. Introduction

In Austria the Ostrong Nappe System is part of the Moldanubian Nappes (Bohemian Massif). This Nappe System comprises mainly paragneisses but further hosts several intercalations of orthogneiss. These orthogneiss bodies have been identified (Graf, 2017) as the source of topaz in stream sediments (Göd, 1988, 1989) at the eastern slope of the Ostrong in Lower Austria (Fig. 2). So

far, these are the only occurrence of topaz-bearing orthogneiss within the entire Bohemian Massif in Austria. However, the characteristics and genesis of this gneiss remained largely unclear. This contribution provides a comprehensive study of the orthogneiss bodies, which were characterized by petrological, geochemical as well as structural methods. Furthermore, in-situ U-Pb dating of zircon was used to determine the protolith age of the

gneiss constraining the first minimum sedimentation age for rocks of the Ostrong Nappe System. In conclusion, we compare our geochemical and geochronological results with those of other metagranitoids and orthogneisses of the Moldanubian Nappes and discuss the genesis of the orthogneiss from the Ostrong Nappe System in this tectonic framework.

2. Regional geology

The Bohemian Massif in Austria consists of the Moravian and Moldanubian Superunits, formed during the Variscan orogenic event (Suess, 1911; Tollmann, 1982; Franke, 2000). The Moldanubian Superunit can be subdivided into the South and Central Bohemian Batholiths, the Bavarian Massif as well as the Moldanubian Nappes (Fig. 1). The latter is built by three nappe systems (Linner, 2013) characterized by their different lithology and metamorphic evolution, with an increasing metamorphic grade from the footwall Ostrong Nappe System (N.S.) to the overlying Drosendorf N.S. and the hanging wall Gföhl N.S. (Petrakakis, 1997).

The Gföhl N.S. consists of various migmatic orthogneiss, paragneiss, granulite, amphibolite, eclogite and peridotite (Petrakakis, 1997; Fuchs et al., 1990; Lindner & Finger, 2018). This unit underwent eclogite-facies and partly ultrahigh-pressure peak metamorphic conditions (Kotková, 2007; Perraki and Faryad, 2014; Schantl et al., 2019) followed by high-pressure granulite-facies conditions, interpreted as continental subduction during the Variscan orogeny, followed by rapid exhumation (Carswell, 1991; Schulmann et al., 2005). Granulite-facies

peak metamorphic conditions followed by a low-pressure overprint (Högelsberger, 1989; Petrakakis, 1997) are characteristic for the Drosendorf N.S., which consists of paragneiss, quartzite, marble, graphitic schist, amphibolite, calc-silicate rocks and orthogneiss (Fuchs et al., 1990; Racek et al., 2006; Lindner and Finger, 2018). The provenance of this unit shows strong affinities to Avalonia (Finger and Schubert, 2015; Lindner et al., 2021).

The lowermost tectonic unit is the Ostrong N.S.. The dominant lithology is paragneiss, subdivided into cordierite-sillimanite gneiss and cordierite-free biotite-plagioclase gneiss (Fuchs and Fuchs, 1986; Linner, 1996). Calc-silicate rocks, quartzite, eclogite, amphibolite and orthogneiss are also present. This unit underwent granulite-facies low-pressure metamorphic conditions (Petrakakis, 1997; Lindner and Finger, 2018). Linner (1996) divides the evolution of the Ostrong N.S. into 3 metamorphic stages. An early stage with a maximum temperature of 600 °C is inferred from kyanite relics in cordierite gneiss and relict kyanite-staurolite intergrowths in garnet-bearing paragneiss. The peak stage is around 720 °C and more than 4.4 kbar, followed by a retrograde stage at about 650–700 °C and 3–5 kbar, with post-deformation white mica growth. The investigated area is part of the Ostrong N.S. and we especially focus on "leucocratic gneiss commonly bearing sillimanite" as described by Fuchs and Fuchs (1986), which is found as several bodies in the southern to middle parts. In the more western areas this gneiss appears as rather circular bodies with a lateral extension from about 50 to 1500 m. We describe these occurrences as Type 1 (Tab. 1). In the easternmost parts near the tectonic boundary to the Drosendorf N.S.

| Sample	Lithology	Laimbach Orthogneiss Lithodem Type	Coordinates	Outcrop type
VM19-1	Orthogneiss	Type 1	48°17'03''N; 15°08'04''E	boulder
VM19-2	Orthogneiss	Type 1	48°17'15''N; 15°08'32''E	boulder
VM19-4	Orthogneiss	Type 1	48°17'18''N; 15°08'35''E	boulder
VM19-5	Orthogneiss	Type 1	48°17'43''N; 15°07'51''E	boulder
VM19-6	Orthogneiss	Type 1	48°17'22''N; 15°07'29''E	in situ
VM19-7	Orthogneiss	Type 1	48°17'34''N; 15°07'15''E	in situ
VM19-8	Orthogneiss	Type 1	48°18'14''N; 15°07'52''E	in situ
VM19-9	Orthogneiss	Type 1	48°18'23"N; 15°08'20''E	boulder
VM19-10	Orthogneiss	Type 1	48°18'22"N; 15°08'23"E	boulder
VM19-14	Orthogneiss	Type 1	48°17'38"N; 15°07'13"E	in situ
VM19-16	Orthogneiss	Type 1	48°17'38"N; 15°07'13"E	in situ
VM19-17	Orthogneiss	Type 1	48°17'38"N; 15°07'14"E	in situ
VM19-18	Orthogneiss	Type 1	48°17'04"N; 15°08'06''E	boulder
VM19-19	Orthogneiss	-	48°21'54"N; 15°07'33''E	boulder
AM19-23	Orthogneiss	Type 2	48°18'37''N; 15°12'44''E	in situ
AM19-24	Orthogneiss	Type 2	48°20'01''N; 15°12'22''E	boulder
AM19-25	Orthogneiss	Type 1	48°19'59''N; 15°07'31''E	boulder
AM19-26	Orthogneiss	Type 1	48°21'11''N; 15°08'09''E	boulder

Table 1:
Listing of the samples.
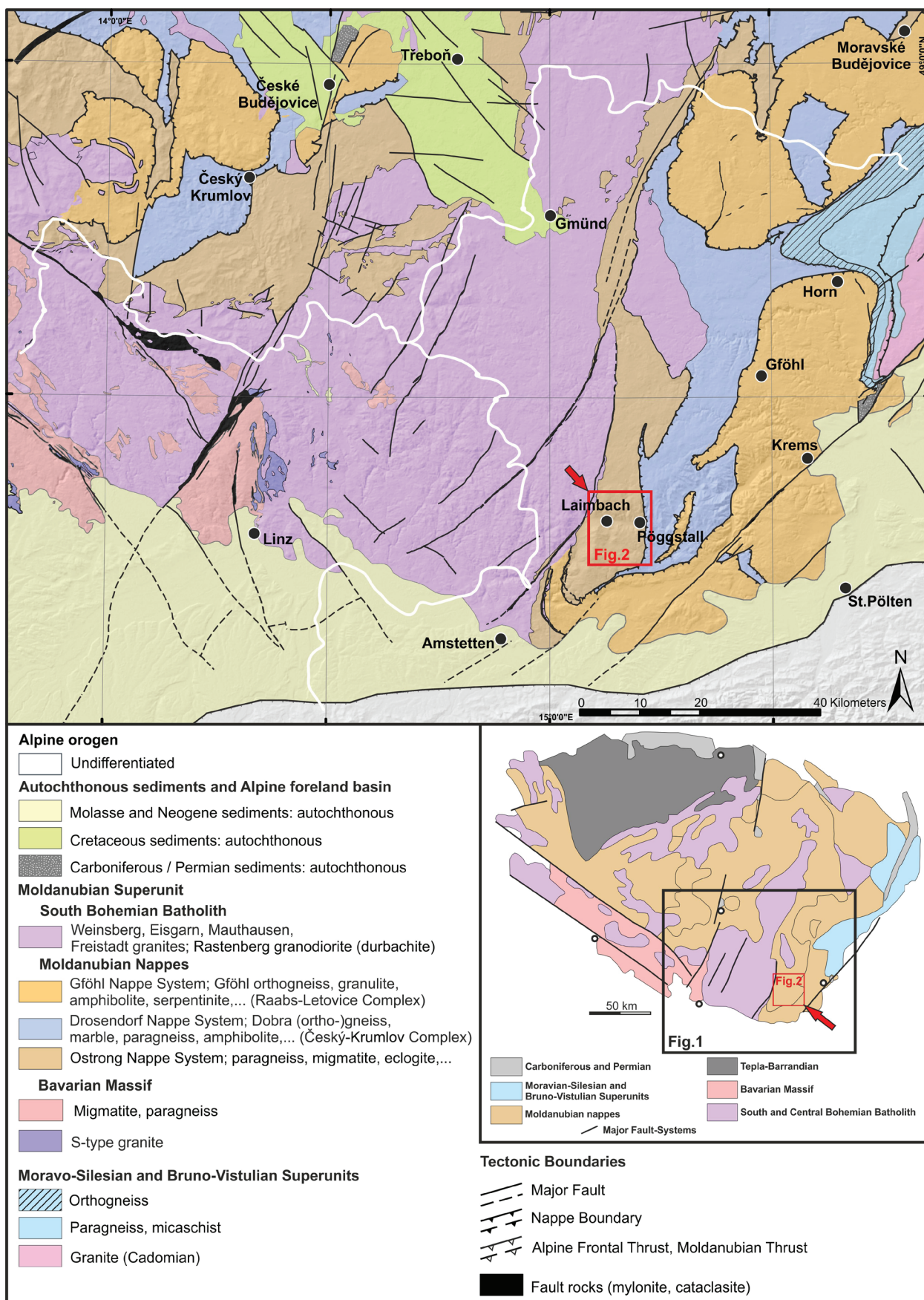
Figure 1: Geological overview of the Bohemian Massif based on Schnabel et al. (2002), Krenmayr et al. (2006) and Cháb et al. (2007). The overview map is based on Wallbrecher et al. (1996), Brandmayr et al. (1999), Büttner (2007), Cháb et al. (2007) as well as Kroner and Romer (2013). The investigated area (Fig. 2) is marked by a red arrow and square. Federal boundaries are in white.

the orthogneiss appears as narrow, elongated bodies with a width of 50 m and length of 200 to about 3500 m on average. These occurrences are described as Type 2 (Tab. 1).

3. Methods
3.1 Whole-rock geochemistry
The analyses for major and trace elements have been performed on a sequential X-ray spectrometer PHILIPS PW2404 at the Department of Lithospheric Research, University of Vienna. A super-sharp end-window tube with a Rh-anode and a programmable 4 kW generator (60 kV max., 125 mA max.; iso-Watt-switching) have been used together with the software PANalytical "SuperQ" vers. 5.1B (5.2822.3) with the options "Pro-Trace" and "Omnian". Major elements were analysed on calcined rock powder fused with lithium tetraborate/metaborate as flux to form a glass bead and trace elements directly on the crushed and milled rock powder mixed with poly-vinyl alcohol as a binding agent to form a pressed powder pellet.

Trace elements, which could not be determined with X-ray fluorescence (XRF) or only with insufficient detection limits, have been analysed by ALS Minerals in Loughrea, Ireland using a sodium peroxide fusion by inductively coupled plasma mass spectrometry (ICP-MS). Boron was determined by ICP-MS using glassless equipment to avoid contamination. Fluorine was detected by Ion Chromatography with potassium hydroxide fusion.

3.2 Mineral chemistry
A CAMECA SXFiveFE electron probe micro-analyser (FEG-EPMA) at the Department of Lithospheric Research, University of Vienna, was used to analyze mineral compositions. It is equipped with a FEG Schottky type field-emission gun electron source and with five crystal spectrometers for wavelength dispersive elemental analysis. For the measurements the instrument was run with an accelerating voltage of 15 kV and a probe current of 20 nA. Plagioclase and K-feldspar compositions were analysed with a defocused beam of 5 µm diameter, all other compositions with a focused beam of <1 µm diameter.

3.3 Raman spectroscopy
Micro-spectroscopy was done at the Department of Mineralogy and Crystallography, University of Vienna, using a Horiba LabRAM HR Evolution system equipped with Olympus BX-series optical microscope and Peltier-cooled, Si-based charge-coupled device detector. Laser-induced photoluminescence (PL) spectrum and Raman spectrum in the "lattice" region were excited with the 532 nm emission of a frequency-doubled Nd-YAG laser (12 mW at the sample), and the Raman spectrum in the O–H stretching region was excited with the 633 nm emission of a He-Ne laser (10 mW). A 100× objective (numerical aperture 0.90)

was used to focus the light onto the sample surface. The light to be analysed was dispersed with a 1800 grooves per mm diffraction grating. More experimental details are described elsewhere (Zeug et al., 2018). Topaz was identified by micro-spectroscopy, first from the characteristic fingerprint pattern of Raman-active vibrations, and second from the characteristic PL fingerprint pattern of emissions of trace Cr^{3+}.

3.4 LA-ICP-MS U-Pb zircon dating
Zircon grains were separated at the Department of Lithospheric Research, University of Vienna, by gravity and heavy liquid separation. This separation was followed by handpicking of various grains, mounting in epoxy resin and subsequent polishing. These mounts were coated with gold at the Geological Survey of Austria in Vienna and imaged using a VEGA/TESCAN scanning electron microscope, equipped with a 50 mm² Oxford detector. Images with cathodoluminescence and secondary electrons were taken to visualize the zoning of the zircons. This allowed determination of desired areas for U-Pb age dating. Laser ablation inductively coupled plasma mass spectrometry (LA-ICP-MS) U-Pb age dating was done at the Institute of Geology of the Czech Academy of Sciences in Prague (Czech Republic), where a Thermo Scientific double-focusing magnetic sector field Element 2 HR-ICP-MS coupled to a 193 nm ArF excimer laser (Teledyne Cetac Analyte Excite laser) was used. The laser conditions were set to a repetition rate of 5 Hz, 22–25 µm spot size and fluence of 3.53 J/cm². The description of the instrument and the analytical procedure are given in Soejono et al. (2019). IsoplotR (Vermeesch, 2018) was used to plot U-Pb data in Tera-Wasserburg diagrams and calculate final mean ages.

4. Results
In the present work, the orthogneiss bodies are collectively grouped under the term Laimbach Orthogneiss. We further suggest defining herewith the *Laimbach Orthogneiss Lithodeme*, named after the locality Laimbach am Ostrong (48°19′01″N; 15°07′19″E).

4.1 Petrography of the Laimbach Orthogneiss
4.1.1 Macroscopic description
We investigated 18 orthogneiss samples from different localities and with different modes of occurrence. The rock is a fine- to medium-grained leucocratic bright gneiss with a weak to well-developed foliation and local open to isoclinal folding. Although, this orthogneiss is relatively homogeneous we suggest to discriminate between two types, based on their position within the Ostrong N.S.: Type 1 for the central and western parts and Type 2 for the easternmost parts near the tectonic boundary to the Drosendorf N.S.. For both types no contacts to the adjacent rocks have been observed in the field.
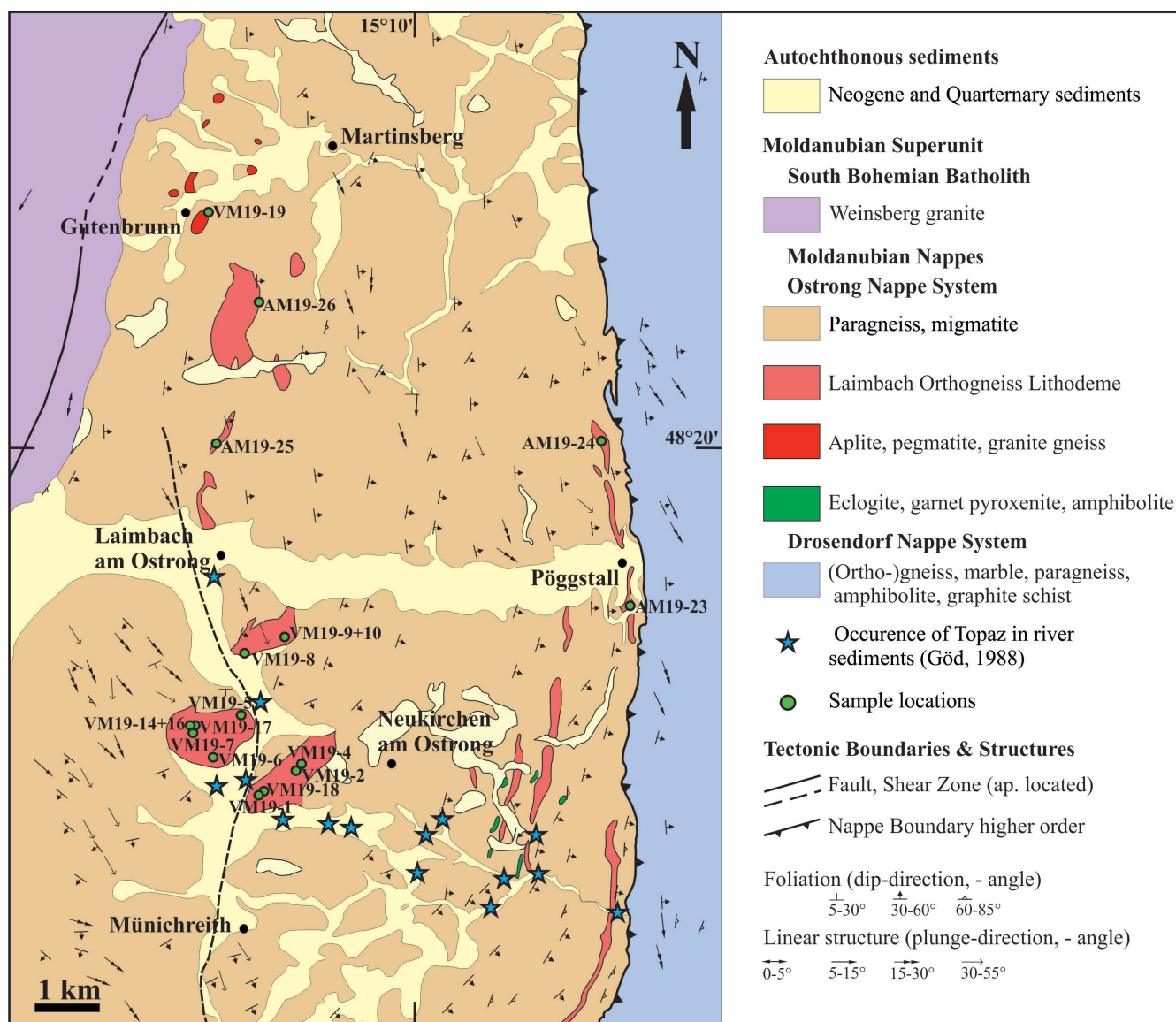
Figure 2: Simplified geological map of the investigated area. The locations of the samples are indicated by the green dots. Structural features are modified after Fuchs and Fuchs (1986).

We collected one orthogneiss sample (VM19-19) from the lithology mapped as "Aplite, pegmatite, granite gneiss" (Fig. 2) in the Ostrong N.S. in order to distinguish it from the Laimbach Orthogneiss. As confirmed by further analyses the lithology "Aplite, pegmatite, granite gneiss" (Fig. 2) is different from the Laimbach Orthogneiss.

The macroscopic appearance of Type 1 Laimbach Orthogneiss is blocky and mostly strongly weathered (Fig. 3a). The foliation is weak to well developed and varies only slightly between the different occurrences. The main foliation dips towards east-southeast with dip angles around 30–60°, which is basically the same for the surrounding paragneiss. Furthermore, it shows local folding of felsic, partly discordant layers (Fig. 3b-c). On average 1–4 cm sized whitish to pinkish, rarely yellowish and greenish nodular mineral aggregates of sillimanite and quartz showing a positive weathering on the rock surfac-

es are abundant (Fig. 3a-b). The mineral aggregates do not only occur on weathered rock surfaces, but are distributed throughout the rock.

Type 2 Laimbach Orthogneiss (Fig. 3d) is just as blocky and mostly strongly weathered as Type 1. The main foliation dips towards east with dip angles around 40–80°, which correlates with the structure of the surrounding paragneiss. The distinctive difference between the two types is that Type 2 shows a stronger degree of deformation with distinctive mylonitic foliation and stretching lineation (Fig. 3d-f).

4.1.2 Microscopic description

Type 1 shows the mineral assemblage quartz + K-feldspar + plagioclase + biotite + opaque phases ± white mica ± sillimanite ± garnet ± zircon (Fig. 4a-b, Fig, 4e-f). The
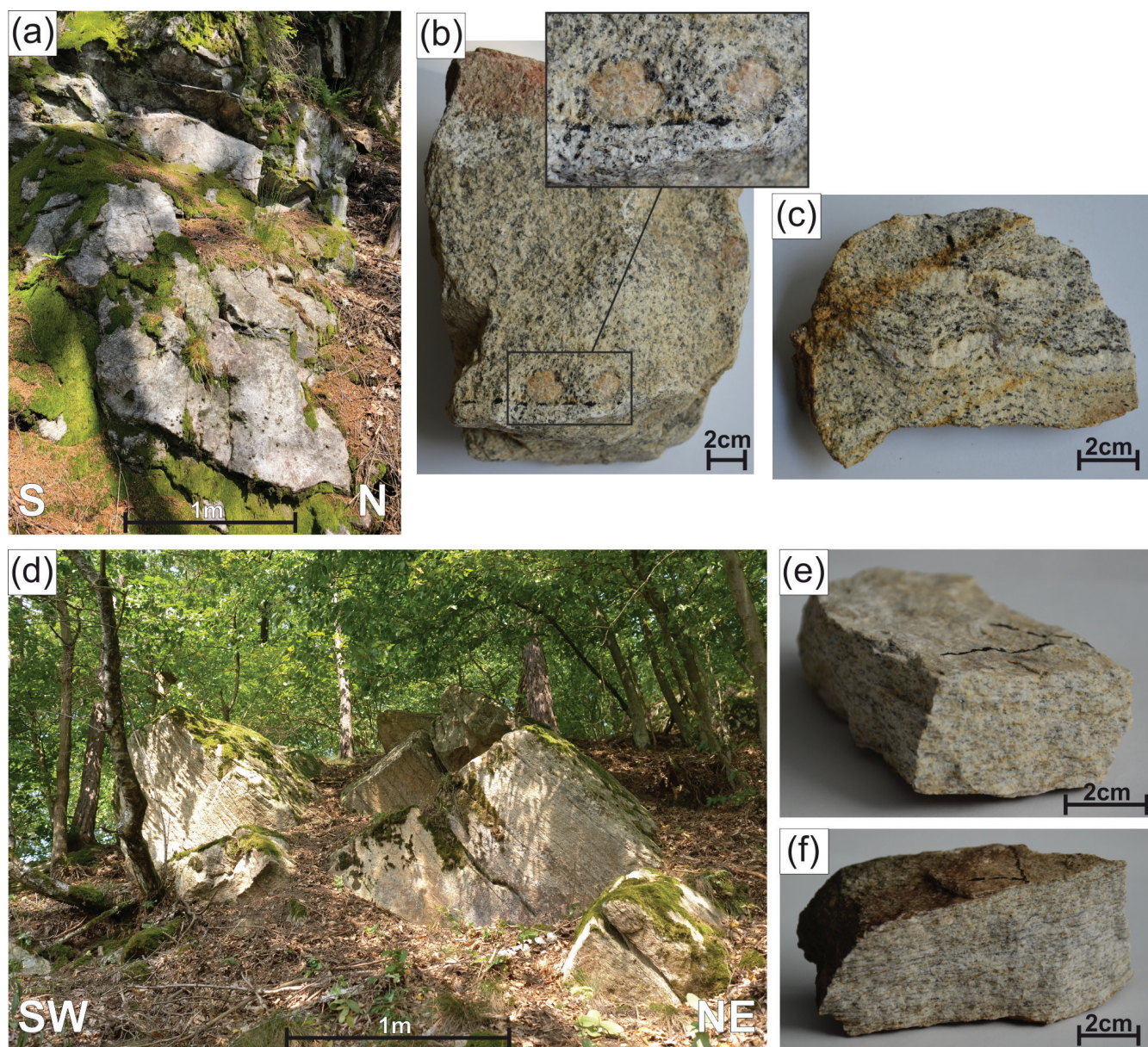
Figure 3: (a) Typical outcrop of Type 1 (VM19-17 sample location) and photographs of Type 1 hand specimens showing (b) VM19-9 with sillimanite-quartz-aggregates in detail and (c) VM19-5 with indicated folding. (d) Typical outcrop of Type 2 (AM19-23 sample location) and photographs of Type 2 hand specimens showing (e) AM19-23 and (f) AM19-24 with both a distinctive mylonitic foliation and stretching lineation.
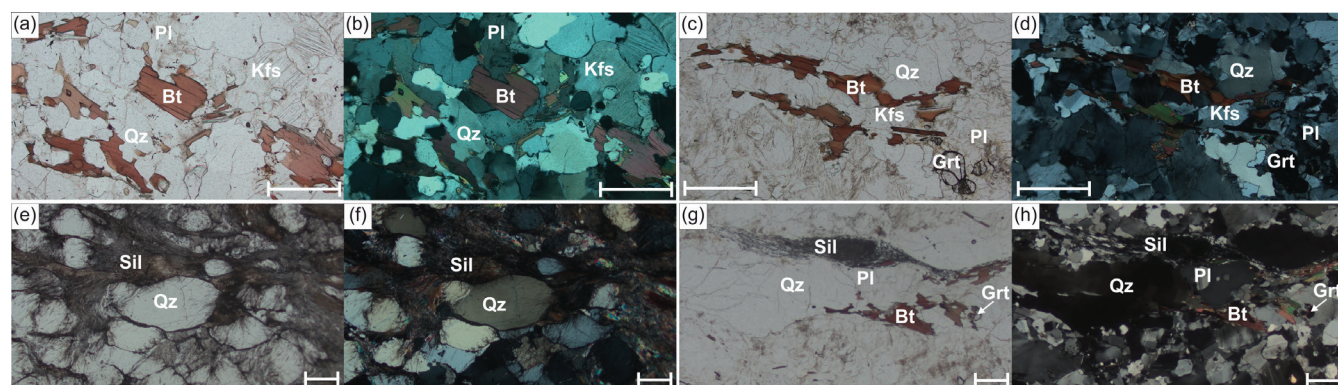
Figure 4: Photomicrographs of selected samples. (a), (b) shows rock structure of sample AM19-25 as example for Type 1 in (a) plane- and (b) cross-polarized light (c), (d) shows rock structure of sample AM19-23 as example for Type 2 in (c) plane- and (d) cross-polarized light. (e), (f) shows sillimanite-quartz aggregates of Type 1 in sample VM19-14 in (e) plane- and (f) cross-polarized light. (g), (h) shows sillimanite-quartz aggregates of Type 2 in sample AM19-23 in (g) plane- and (h) cross-polarized light. The scale bars represent 500 μm.

ratios of quartz (~35–40 vol%), K-feldspar (~30–35 vol%) and plagioclase (~20–25 vol%) to each other are constant. K-feldspar regularly shows perthitic segregation and appears as microcline. Plagioclase shows polysynthetic twinning and locally the formation of myrmekites is observed. Biotite and white mica are xenomorphic to hypidiomorphic and occur in different vol% in the different samples. They occur mostly grouped, in layers and clusters. Occasionally, white mica porphyroblasts occur, which are not foliated and overgrow grain boundaries. Garnet is single-phased and hypidiomorphic and occurs only rarely and mostly with average grain sizes of 0.1-0.2 mm. Only in sample VM19-10 it occurs more frequently. In sample VM19-10, besides smaller garnet, there are also large, partly fragmented porphyroblasts, about 0.3-0.5 cm in diameter. The nodular mineral aggregates (Fig. 3b) consist of sillimanite and quartz (Fig. 4e-f). Sillimanite occurs as fibrolite and is in places prismatic. It grows around quartz and sometimes sillimanite needles penetrate into the quartz. Apart from that, smaller sillimanite clusters are also found at distance from the aggregates throughout the rock. Opaque phases occur to a lesser extent, as well as accessory apatite and zircon.

The mineral assemblage of Type 2 is quartz + K-feldspar + plagioclase + biotite + sillimanite + kyanite + garnet + opaque phases (Fig. 4c-d, Fig. 4g-h). Characteristically no white mica is present. Quartz (~35–40 vol%) is dynamically recrystallized by grain boundary migration. Up to mm-large K-feldspar (~30–35 vol%) and plagioclase (~25–30 vol%) recrystallized into small grains suggesting dynamically recrystallization by subgrain rotation. Plagioclase shows frequent polysynthetic twinning and K-feldspar perthitic exsolution. Biotite is predominantly arranged in layers parallel to the foliation. With an average size of 0.1-0.2 mm in diameter, garnet is hypidiomorphic and single-phased. Kyanite occurs rarely. The nodular sillimanite-quartz-aggregates from Type 1 orthogneiss are also found in Type 2, but they are thin and elongated parallel to the foliation (Fig. 4g-h). The strongest deformation is seen in Type 2 orthogneiss. Quartz is characterized by grain boundary migration and was deformed into elongated grains recording a shape preferred orientation (SPO). Inspection with the tint plate suggests that the dynamically recrystallized quartz records a crystal preferred orientation (CPO). Feldspar recrystallized into a smaller grain size by subgrain rotation.

Sample VM19-19 (orthogneiss from "Aplite, pegmatite, granite gneiss" occurrences, Fig. 2) shows the mineral assemblage quartz + K-feldspar + plagioclase + biotite + garnet + opaque phases ± zircon. Garnet is frequent and about 0.1-0.5 mm in size. Compared to the Laimbach Orthogneiss, white mica (only present in Type 1) and sillimanite as well as the sillimanite-quartz-aggregates are completely absent.

Topaz could not be identified macroscopically or petrographically, but with further investigations in heavy mineral concentrates using Raman spectroscopy (see Chapt. 4.4).

4.2 Geochemistry

Ten samples were analysed and the results are shown in Table 2–3. Plotting the data in the TAS classification diagram after Middlemost (1994) suggests that all samples can be classified as former granites (Fig. 5a). Furthermore, all samples uniformly possess a peraluminous
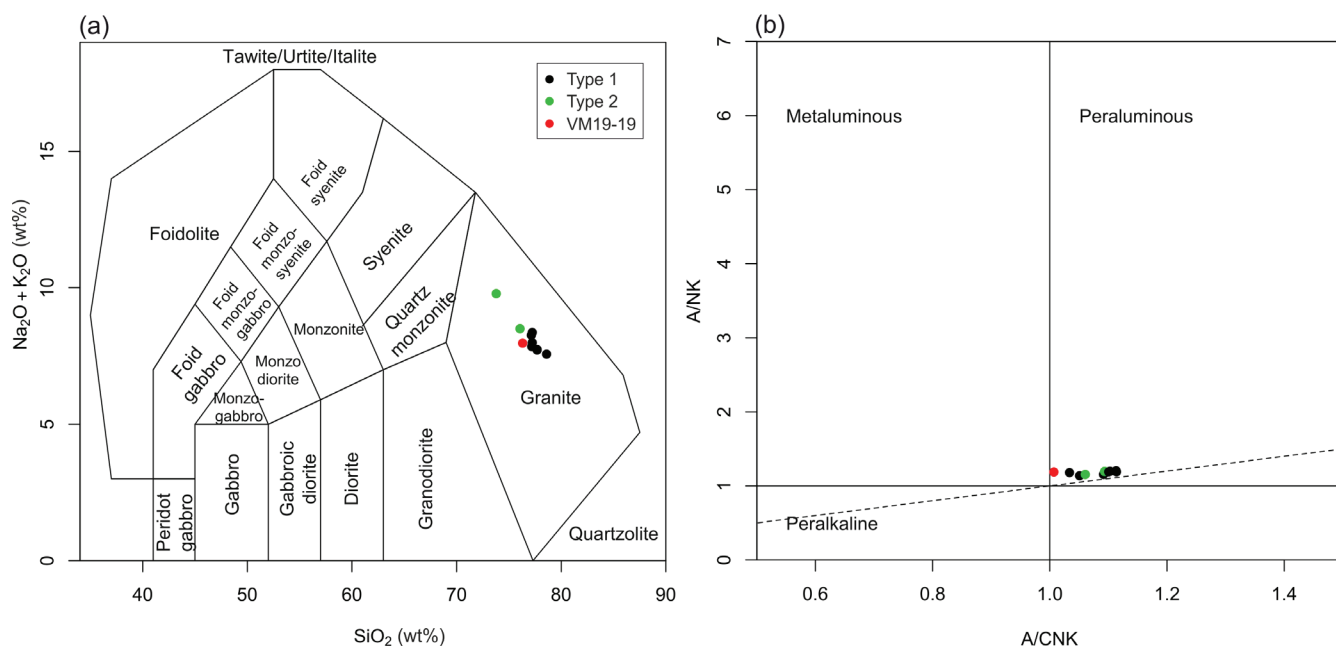

Figure 5: (a) Total Alkali vs Silica (TAS) classification diagram of plutonites after Middlemost (1994) and (b) A/CNK vs. A/NK diagram of peraluminosity after Shand (1943). A/NK = Al_2O_3 / ($Na_2O + K_2O$) (molar ratio).

Sample	VM19-2	VM19-8	VM19-10	VM19-14	VM19-16	VM19-18	VM19-19	AM19-23	AM19-24	AM19-25
Type	Type 1	Type 1	Type 1	Type 1	Type 1	Type 1	-	Type 2	Type 2	Type 1
SiO$_2$ [wt%]	77.11	76.10	77.25	76.80	75.77	76.54	75.08	72.84	75.09	76.78
TiO$_2$	0.14	0.11	0.12	0.14	0.12	0.09	0.21	0.09	0.10	0.14
Al$_2$O$_3$	11.61	11.89	11.14	12.07	12.02	12.22	12.15	14.41	13.26	11.64
Fe$_2$O$_3$	1.76	1.35	1.21	1.75	1.56	1.54	1.86	0.69	0.87	1.72
MnO	0.03	0.01	0.04	0.03	0.03	0.02	0.03	0.01	0.02	0.04
MgO	0.24	0.15	0.28	0.25	0.16	0.09	0.18	0.13	0.17	0.24
CaO	0.46	0.48	0.74	0.46	0.38	0.34	1.01	0.61	0.57	0.44
Na$_2$O	2.45	2.71	2.45	2.76	2.87	3.02	3.10	3.59	3.57	2.70
K$_2$O	5.23	5.53	4.99	5.05	4.97	5.18	4.74	6.07	4.82	4.93
P$_2$O$_5$	0.22	0.21	0.07	0.20	0.22	0.18	0.04	0.28	0.26	0.20
LOI	0.46	0.27	0.21	0.28	0.32	0.35	0.26	0.27	0.24	0.32
Total	99.71	98.81	98.50	99.79	98.42	99.57	98.66	98.99	98.97	99.15

Table 2: Whole-rock major element geochemistry data from the orthogneiss samples. LOI = loss on ignition.

character (Fig. 5b) and comparably low Sr content of ca. 30–130 ppm. It is also emphasized by the Rb/Sr ratio from Type 1 (1–17) and from Type 2 (1–2), which is elevated with respect to the Rb/Sr ratio of 0.15 of the bulk continental crust (Rudnick and Gao, 2005). The protolith of the orthogneiss is thus classified as S-type granite. The K/Rb ratio from Type 1 is low (78–246) and that of Type 2 is elevated (326–352) compared to the bulk continental crust (304; Rudnick & Gao, 2005). The U/Th ratio varies from 0.31 to 0.59 for Type 1 and 0.90 to 1.60 for Type 2, which is elevated compared to the bulk continental crust (0.23; Rudnick and Gao, 2005). F (340–2760 ppm Type 1, 470–2540 ppm Type 2) and W (6.9–51.7 ppm Type 1, 21.9–37.2 ppm Type 2) are enriched compared to the bulk continental crust with 553 ppm F and 1 ppm W (Rudnick and Gao, 2005). On a chondrite-normalized REE diagram (Fig. 6a) the samples show flat, nearly parallel trends and light rare earth element (LREE) as well as heavy rare earth element (HREE) enrichment. Samples AM19-23 and AM19-24, which represent Type 2 Orthogneiss, show a positive Eu anomaly, whereas all other samples, which represent Type 1 Orthogneiss, show a negative Eu anomaly. In general, Type 2 samples show slight geochemical variation from the Type 1 samples. Incompatible elements such as REE and Zr are lower in Type 2 compared to Type 1 (Fig. 6a-b). Furthermore, Type 2 rocks show the highest K/Rb and U/Th ratios from all samples.

Sample VM19-19 as an orthogneiss representative for the occurrences of the "Aplite, pegmatite, granite gneiss" lithology (Fig. 2) in the Ostrong N.S. shows slight geochemical differences in comparison with Type 1 and 2 samples. VM19-19 has for example higher concentrations of incompatible elements such as REE and Zr as well as higher Sr contents while its K/Rb ratio is between those of Type 1 and 2 (Fig. 6a-b). Ba in VM19-19 is, together with Type 2, higher than Type 1. Regarding the major element
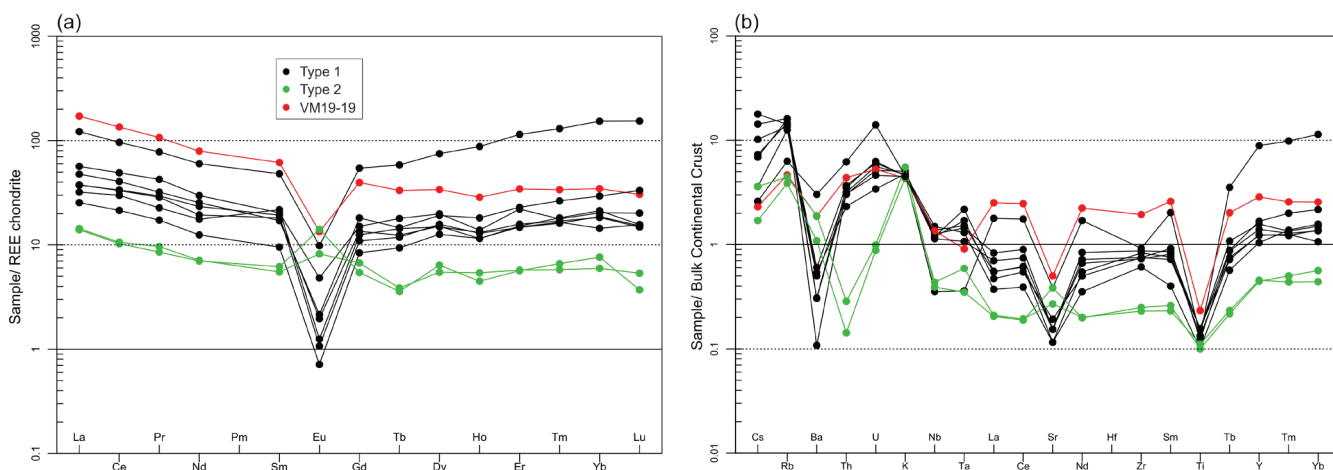

Figure 6: (a) Chondrite-normalized rare earth element (REE) concentrations after Anders and Grevesse (1989) and (b) trace element spider diagram with values normalized to the bulk continental crust after Taylor and McLennan (1995).

Sample	VM19-2	VM19-8	VM19-10	VM19-14	VM19-16	VM19-18	VM19-19	AM19-23	AM19-24	AM19-25
Type	Type 1	Type 1	Type 1	Type 1	Type 1	Type 1	-	Type 2	Type 2	Type 1
Ag [ppm]	<5	<5	<5	5	<5	<5	5	<5	<5	<5
As	<4	<4	<4	<4	<4	<4	<4	<4	<4	<4
Ba	135	125	757	151	77	27	468	472	272	76
Be	0.9	0.4	1	1.2	1	0.6	2.5	<0.4	<0.4	0.6
Bi	0.1	0.1	0.2	0.3	0.1	0.4	0.2	0.2	0.2	0.1
Cd	<0.8	0.8	0.8	1.1	0.8	0.9	1	1	1	<0.8
Ce	20	18	58	29.6	20.3	12.9	81.4	6.2	6.4	24.5
Co	5.2	13	5.7	3.8	5.6	6	2.8	5.3	3.6	5.9
Cs	10.2	3.6	2.6	17.8	14.3	6.9	2.3	3.6	1.7	7.3
Cu	<20	<20	<20	<20	<20	<20	<20	<20	<20	<20
Dy	3.66	3.62	18.2	4.81	3.83	3.07	8.24	1.55	1.33	4.64
Er	2.36	2.51	18.2	3.51	2.34	2.41	5.46	0.9	0.91	3.64
Eu	0.11	0.07	0.55	0.27	0.06	0.04	0.75	0.79	0.46	0.12
Ga	19.9	20.1	13.7	21.5	22.5	22.3	22.9	12.8	13.5	21.1
Gd	2.65	2.45	10.7	2.96	2.15	1.65	7.8	1.07	1.32	3.57
Ge	2.9	3.2	2.9	2.9	2.9	2.8	2.2	2.4	2.9	3
Ho	0.64	0.73	4.88	0.77	0.72	0.64	1.59	0.25	0.3	1.01
In	<0.3	<0.3	<0.3	<0.3	<0.3	<0.3	<0.3	<0.3	<0.3	<0.3
K	40500	45000	41700	42200	40700	42000	36600	50000	40300	40300
La	8.87	7.54	28.6	13.3	8.76	5.96	40.3	3.28	3.36	11.2
Li	117	32	16	103	122	65	16	16	32	65
Lu	0.38	0.36	3.75	0.49	0.37	0.38	0.74	0.09	0.13	0.81
Mo	<2	<2	<2	<2	<2	<2	<2	<2	<2	<2
Nb	13.1	13	3.9	13.9	15.1	16.4	14.9	4.3	4.8	12.5
Nd	8.76	7.97	27.2	13.45	10.55	5.64	35.8	3.17	3.22	11.5
Ni	10	10	10	10	10	10	20	150	10	10
Pb	8.2	5.9	21.4	5.4	6.3	6.1	20	42.5	29.8	7.4
Pr	2.55	2.02	6.95	3.79	2.63	1.54	9.53	0.76	0.86	2.86
Rb	434	402	201	454	519	506	149	142	123.5	469
Re	<0.01	<0.01	<0.01	<0.01	<0.01	<0.01	<0.01	<0.01	<0.01	<0.01
Sb	<0.3	0.7	0.7	<0.3	<0.3	<0.3	<0.3	<0.3	<0.3	<0.3
Se	3	9	4	8	5	<3	7	7	7	<3
Sm	2.66	3.2	7.09	2.99	2.83	1.4	9.08	0.91	0.81	2.52
Sn	8	6	5	10	9	8	4	4	3	13
Sr	30	50	100	40	40	30	130	100	70	40
Ta	2.18	1.7	0.36	1.44	1.52	1.3	0.91	0.35	0.59	1.07
Tb	0.45	0.52	2.12	0.65	0.43	0.34	1.21	0.13	0.14	0.53
Te	0.6	<0.5	<0.5	<0.5	<0.5	<0.5	<0.5	<0.5	<0.5	<0.5
Th	8.1	10.6	21.7	12.9	12.3	11.1	15.3	1	0.5	10.7
Tl	2.26	1.66	1.02	2.31	2.63	2.1	0.7	0.59	0.56	1.95
Tm	0.4	0.41	3.15	0.43	0.39	0.44	0.82	0.16	0.14	0.64
U	3.1	4.7	12.8	5.5	5.7	5.1	4.8	0.9	0.8	4.2
V	6	5	7	9	7	4	10	6	5	7
W	8.3	51.7	28	13.1	38.9	43.3	6.9	37.2	21.9	39.4
Y	24.5	28	177.5	31.4	24.9	20.9	57.3	8.9	9.1	33.4
Yb	2.34	2.98	25	3.3	3.04	3.46	5.63	1.24	0.97	4.77
Zn	50	40	30	50	50	50	50	30	30	60
B	19	20	18	26	31	23	25	37	28	31
F	2480	2270	490	1070	2410	2590	2760	2540	470	340
Cr	12	6	8	10	10	7	9	13	9	11
Sc	3	1	4	4	4	5	4	2	2	5
Zr	83	75	92	87	73	61	194	25	23	75
K/Rb	93	112	207	93	78	83	246	352	326	86
U/Th	0.38	0.44	0.59	0.43	0.46	0.46	0.31	0.90	1.60	0.39
Rb/Sr	14	8	2	11	13	17	1	1	2	12
A/CNK	1.10	1.05	1.03	1.11	1.11	1.09	1.01	1.06	1.09	1.10

Table 3: Whole-rock trace element geochemistry data from the orthogneiss samples. A/CNK = Al_2O_3 / (K_2O + Na_2O + CaO) (molar ratio).

composition, VM19-19 lies more or less between Type 1 and 2 with a few outliers like e.g. higher TiO_2 and higher CaO.

Among Type 1 samples, VM19-10 is the only sample with a different geochemistry. VM19-10 shows similarities to sample VM19-19 with for example higher concentrations of incompatible elements such as REE and Zr as well as a higher K/Rb ratio and higher Ba and Sr contents (Fig. 6a-b).

4.3 Mineral chemistry

Representative results of K-feldspar, plagioclase, garnet, biotite and sillimanite analyses are shown in Table 4.

Plagioclase is zoned (Fig. 8a-b, Tab. 4) with an albite component of about 87–99 mol%, increasing towards the grain margin. K-feldspar has a low albite component of about 5–16 mol%. Garnet shows no chemical zoning (Fig. 8c-d, Tab. 4) and is Fe-dominated with 82–86 mol% almandine, ca. 9–13 mol% pyrope, spessartine ca. 3–5 mol%, and grossular < 2 mol%. Biotite is classified as Fe-biotite in Type 1 and Fe-/Mg-biotite in Type 2 (sample AM19-23) (Fig. 9a) as well as annite to siderophyllite (Fig. 9b) following the classification of Deer et al. (2001). In general, X_{Mg} varies from 0.09 to 0.39 (Tab. 4) and is highest in Type 2 Laimbach Orthogneiss. Selected measurements of the nodular sillimanite-quartz aggregates are presented in Table 4. In combination with petrographic investigations the alumosilicate is clearly identified as sillimanite.

4.4 Raman spectroscopy

Samples VM19-14, VM19-17 and AM19-25 have been analysed with Raman spectroscopy and topaz was identified in all three samples. The Raman spectrum from a topaz from VM19-14 (Fig. 10a–b) is shown in Figure 10c (for details of the band assignment see Beny and Piriou, 1987). The O–H stretching range is dominated by a narrow band at ~3650 cm^{-1}, which corresponds to "OH$_B$" of Pinhero et al. (2002); with a low-intensity shoulder near ~3640 cm^{-1} ("OH$_A$"). This O–H-band pattern, along with the generally low O-H intensity, points to high F/OH ratio (Pinhero et al., 2002) and hence characterises the sample as F-rich topaz. The laser-induced PL spectrum (Fig. 10d) has comparably low overall intensity. It is dominated by a narrow doublet in the red range, at ~14,632 and ~14,720 cm^{-1} (~683.4 and ~679.4 nm wavelength, respectively), assigned to the split, spin-forbidden $^2E \rightarrow {}^4A_2$ transition of trace Cr^3 (commonly referred to as R$_1$ and R$_2$ lines). This doublet is superimposed on a broad emission feature in the 12,500–15,500 cm^{-1} (ca. 800–645 nm wavelength) range, which is due to the spin-allowed $^4T_2 \rightarrow {}^4A_2$ transition of Cr^{3+} and vibronic sidebands (Tarashchan et al., 2006). The spectral positions of the two R lines correspond to Cr^{3+} in a fully fluorinated environment (O'Bannon and Williams, 2019), which supports the above interpretation of the sample as F-rich topaz.

4.5 U-Pb zircon dating

All zircons show oscillatory zoning as well as a short prismatic habit with lengths of about 90–250 μm and widths of about 30–80 μm (Fig. 11). Their length/width ratios vary from about 1.7:1 to a maximum of 4:1. Furthermore, they show a CL-dark rim, typical for high U- and trace element contents in zircon. Besides rather uniform cores, some also show metamorphic cores (e.g. zircon Nos. 3 and 81). For most measurements, oscillatory zoned domains were chosen, but some cores were also dated. In a few zircons, an overgrowing dark rim can be seen crossing the inner zone discordantly (e.g., zircon Nos. 81 and 67).

A total of 31 spots on 16 zircons from sample VM19-14 and 19 spots on 14 zircons from sample AM19-25 were analysed. Sample VM19-14 was separated into a fraction of 4 smaller (8 spots) and of 12 larger (23 spots) zircons. This separation was necessary in order to obtain the ideal polish plane of the zircons of different sizes, which can only be achieved by a separate process of preparation and dating. The results of the measurements are shown in Figure 11, for all data see Table 5. In our case, the ages of the small and large zircon fraction of sample VM19-14 coincide within the assigned analytical uncertainties.

All analyses have Th/U ratios from 0.03 to 1.03 and apparent $^{206}Pb/^{238}U$ ages ranging from ca. 259 to 628 Ma for sample VM19-14 and ca. 405 to 3002 Ma for sample AM19-25. Apparent $^{206}Pb/^{238}U$ ages of the core zones for sample VM19-14 range from ca. 523 to 628 Ma and from ca. 578 to 3002 Ma for sample AM19-25. The oscillatory mantle zones have apparent $^{206}Pb/^{238}U$ ages ranging from ca. 461 to 613 Ma for sample VM19-14 and ca. 405 to 1669 Ma for sample AM19-25. The only analysis from the rim zone is from sample VM19-14 with the apparent $^{206}Pb/^{238}U$ age ca. 259 Ma. Most $^{206}Pb/^{238}U$ dates cluster around 470–480 Ma from measurements from the oscillatory mantle zones. To calculate the concordia ages we used the analyses from the oscillatory mantle zones, which represent the magmatic or anatectic zircon growth. Single data points older than 510 Ma were not included in the concordia age calculation. The calculations yield the following Tera-Wasserburg concordia ages (Fig. 12): 475.3 ± 1.0 Ma and 474.8 ± 2.9 Ma for sample VM19-14 and 473.5 ± 1.5 Ma for sample AM19-25. The concordia ages correspond well with the $^{206}Pb/^{238}U$ age cluster around 470–480 Ma.

5. Discussion
5.1 Classification of the Laimbach Orthogneiss

Following the North American Stratigraphic Code (NACSN, 2005), we suggest to classify the Laimbach Orthogneiss in the rank of a lithodeme.

The magmatic origin of the gneiss is indicated by major- and trace-element contents. A classification as granite or rhyolite (Fig. 5a) with a peraluminous, S-type character is evidenced. Furthermore, a clear high degree of magmatic differentiation is shown by the high fluorine content, which is largely in the topaz.

	AM19-23	AM19-23	AM19-23	VM19-14	VM19-14	AM19-23	AM19-23	VM19-14	AM19-23	AM19-25	VM19-14	VM19-18	AM19-23	VM19-14	VM19-14	VM19-18
Sample		Type 2		Type 1	Type 1	Type 2	Type 2	Type 1	Type 2	Type 1	Type 1	Type 1	Type 2	Type 1	Type 1	Type 1
Type / Mineral	Grt	Grt	Grt	Pl core	Pl rim	Pl core	Pl rim	Kfs	Kfs	Kfs	Bt	Bt	Bt	Sil	Sil	Sil
														Sil-qz-aggregates	Sil-qz-aggregates	Sil-qz-aggregates
SiO_2	37.08	36.54	36.71	65.58	67.92	64.60	66.98	63.48	63.42	62.19	35.43	34.77	34.89	36.70	36.36	37.01
TiO_2	-0.00	0.00	0.00	0.01	0.00	0.01	0.02	n.a.	n.a.	n.a.	2.20	1.38	3.69	0.00	0.01	0.00
Cr_2O_3	0.01	0.02	0.02	n.a.	n.a.	n.a.	n.a.	n.a.	n.a.	n.a.	0.01	0.01	0.01	0.00	0.00	-0.00
Al_2O_3	21.55	21.47	21.43	21.15	19.92	22.08	20.69	18.97	18.99	19.15	19.61	20.89	19.45	63.43	63.56	62.95
FeO	37.36	37.40	37.51	0.00	0.00	0.02	0.02	0.01	0.02	0.00	24.34	25.02	21.17	0.23	0.26	0.15
MnO	1.42	2.03	1.80	0.01	0.00	0.03	0.03	n.a.	n.a.	n.a.	0.47	0.41	0.07	0.01	0.00	0.00
NiO	n.a.	n.a.	n.a.	n.a.	n.a.	n.a.	n.a.	n.a.	n.a.	n.a.	0.00	0.00	0.01	0.03	0.00	0.00
MgO	3.15	2.50	2.37	0.00	0.01	0.01	-0.00	0.01	0.00	0.01	3.61	1.63	6.84	0.00	0.01	0.00
CaO	0.44	0.52	0.42	1.65	0.20	2.67	0.99	0.02	0.00	0.02	n.a.	n.a.	n.a.	0.00	0.02	0.00
Na_2O	n.a.	n.a.	n.a.	10.62	11.74	10.08	11.24	1.55	1.32	1.22	0.17	0.20	0.12	0.00	-0.00	0.01
K_2O	n.a.	n.a.	n.a.	0.40	0.15	0.38	0.15	14.64	14.82	15.22	9.50	9.26	9.32	0.01	0.00	0.00
Total	101.00	100.44	100.25	99.40	99.93	99.86	100.11	98.67	98.57	97.80	95.33	93.57	95.56	100.39	100.19	100.11
Si	2.97	2.96	2.97	2.90	2.97	2.85	2.93	2.96	2.96	2.94	2.76	2.76	2.67	2.17	2.16	2.20
Ti	-0.00	-0.00	-0.00	0.00	0.00	0.00	0.00				0.13	0.08	0.21	-0.00	0.00	-0.00
Cr	0.00	0.00	0.00	0.00	-0.00	0.00					0.00	0.00	0.00	-0.00	0.00	-0.00
Al	2.03	2.05	2.05	1.10	1.03	1.15	1.07	1.04	1.05	1.07	1.80	1.96	1.75	4.43	4.45	4.40
Fe_{tot}	2.50	2.53	2.54	0.00	0.00	0.00	0.00	0.00	0.00	0.00	1.59	1.66	1.35	0.01	0.01	0.01
Mn	0.10	0.14	0.12	0.00	-0.00	0.00	0.00				0.03	0.03	0.00	0.00	-0.00	0.00
Ni				-0.00							0.00	0.00	0.00	0.00	0.00	0.00
Mg	0.38	0.30	0.29	-0.00	0.00	0.00	-0.00	0.00	0.00	0.00	0.42	0.19	0.78	-0.00	0.00	0.00
Ca	0.04	0.05	0.04	0.08	0.01	0.13	0.05	0.00	0.00	0.00				0.00	0.00	0.00
Na				0.91	1.00	0.86	0.95	0.14	0.12	0.11	0.03	0.03	0.02	0.00	0.00	0.00
K				0.02	0.01	0.02	0.01	0.87	0.88	0.92	0.94	0.94	0.91	0.00	-0.00	0.00
Total	8.01	8.02	8.00	5.01	5.02	5.01	5.01	5.02	5.01	5.04	7.70	7.66	7.70	6.61	6.62	6.60
Alm / Or / X_{Mg}	82.81	83.55	85.01	2.25	0.85	2.09	0.85	86.07	88.09	89.06	0.21	0.10	0.37			
Sps / Ab	3.25	4.71	4.16	90.02	98.23	85.39	94.56	13.85	11.90	10.86						
Pyr / An	12.67	10.20	9.62	7.73	0.92	12.52	4.59	0.08	0.01	0.08						
Grs	1.23	1.49	1.21													

Mineral abbreviations according to Whitney and Evans (2010). n.a. - not analysed

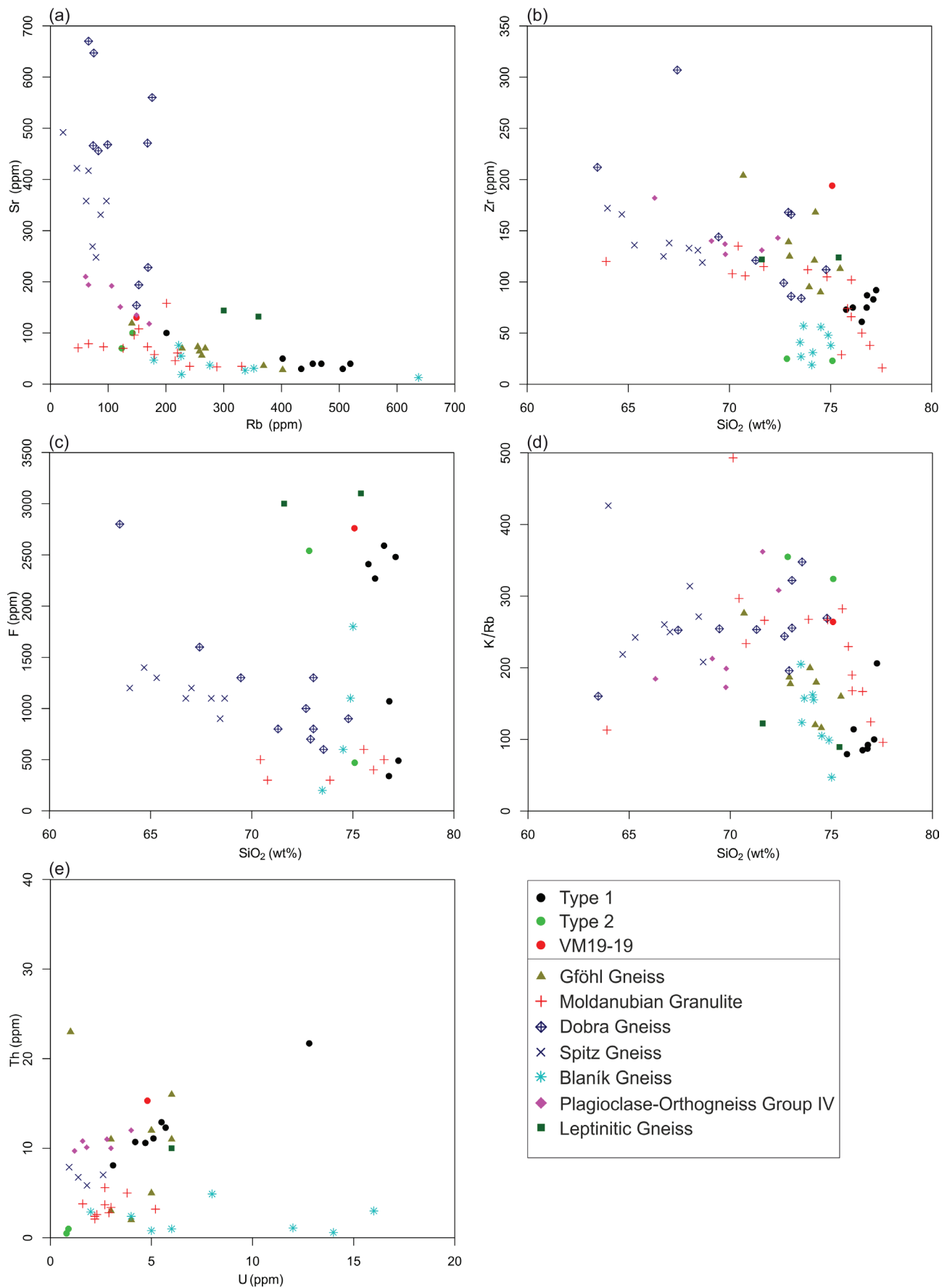**Table 4:** Representative results of mineral analyses from the Orthogneiss.

Figure 7: Harker plots of analysed samples compared with Gföhl Gneiss (René & Finger, 2016), Moldanubian Granulite (Janoušek et al., 2004), Dobra Gneiss (Lindner et al., 2020), Spitz Gneiss (Lindner and Finger, 2018), Blaník Gneiss (René and Finger, 2016), the Plagioclase-Orthogneiss Group IV from Teipel (2003) and Leptinitic Gneiss (Richter and Stettner, 1983). (a) Rb vs Sr; (b) SiO$_2$ vs Zr; (c) SiO$_2$ vs F; (d) SiO$_2$ vs K/Rb; (e) U vs Th.

Sample	Zircon no.	Measuring point	Zircon domain	207Pb/ 235U	±2SE	206Pb/ 238U	±2SE	rho	208Pb/ 232U	±2SE	Pb (ppm)	Th (ppm)	U (ppm)	Th/U	238U/ 206Pb	±2rs (%)	207Pb/ 206Pb	±2rs (%)	206Pb/ 238U age	±2SE
larger fraction:																				
VM19-14	19	19b	core	0.841	0.019	0.102	0.001	0.23	0.032	0.001	23	79	77	1.03	9.77	1.07	0.059	2.36	628.3	6.4
VM19-14	35	35b	mantle	1.860	0.120	0.100	0.002	0.07	0.099	0.010	23	28	80	0.36	10.03	2.21	0.134	6.70	613.0	13.0
VM19-14	24	24a	core	0.723	0.010	0.088	0.001	0.50	0.028	0.001	74	287	980	0.29	11.32	1.12	0.059	1.51	545.7	5.9
VM19-14	04	04a	mantle	0.608	0.009	0.078	0.001	0.49	0.023	0.001	10	45	573	0.08	12.87	1.04	0.057	1.55	482.4	4.8
VM19-14	36	36a	mantle	0.602	0.008	0.077	0.001	0.29	0.023	0.001	6	29	460	0.06	12.91	0.85	0.056	1.49	480.8	4.0
VM19-14	21	21b	mantle	0.603	0.008	0.077	0.001	0.37	0.024	0.001	10	48	379	0.13	12.93	0.80	0.056	1.47	480.2	3.7
VM19-14	19	19a	mantle	0.605	0.008	0.077	0.001	0.27	0.024	0.001	9	42	390	0.11	12.93	0.79	0.057	1.53	480.1	3.6
VM19-14	31	31b	mantle	0.605	0.008	0.077	0.001	0.33	0.025	0.001	15	63	489	0.13	12.96	0.78	0.057	1.48	479.3	3.6
VM19-14	21	21a	mantle	0.612	0.010	0.077	0.001	0.48	0.024	0.001	23	111	462	0.24	12.96	1.00	0.057	1.62	479.2	4.6
VM19-14	02	02a	mantle	0.604	0.009	0.077	0.001	0.46	0.025	0.001	10	46	310	0.15	12.96	0.89	0.057	1.59	479.1	4.1
VM19-14	24	24b	mantle	0.606	0.010	0.077	0.001	0.23	0.026	0.001	8	32	294	0.11	13.02	0.99	0.057	1.75	477.1	4.5
VM19-14	03	03	mantle	0.601	0.010	0.077	0.001	0.22	0.024	0.001	7	35	378	0.09	13.02	0.98	0.057	1.76	477.0	4.5
VM19-14	33	33	mantle	0.598	0.008	0.077	0.001	0.45	0.023	0.001	6	26	400	0.06	13.05	0.93	0.057	1.50	475.9	4.3
VM19-14	32	32b	mantle	0.597	0.008	0.076	0.001	0.33	0.023	0.001	10	47	414	0.11	13.09	0.76	0.056	1.49	474.5	3.5
VM19-14	34	34a	mantle	0.594	0.009	0.076	0.001	0.32	0.023	0.001	15	69	309	0.22	13.13	0.80	0.056	1.58	473.2	3.7
VM19-14	04	04b	mantle	0.602	0.009	0.076	0.001	0.26	0.024	0.001	8	38	432	0.09	13.14	0.88	0.057	1.67	472.7	4.0
VM19-14	34	34b	mantle	0.608	0.009	0.076	0.001	0.49	0.025	0.001	9	39	534	0.07	13.18	0.88	0.058	1.54	471.5	4.0
VM19-14	31	31a	mantle	0.594	0.007	0.076	0.001	0.57	0.024	0.001	12	52	918	0.06	13.18	0.79	0.057	1.29	471.2	3.6
VM19-14	02	02b	mantle	0.593	0.010	0.076	0.001	0.55	0.023	0.001	14	68	722	0.09	13.23	1.24	0.057	1.65	469.7	5.6
VM19-14	32	32a	mantle	0.594	0.010	0.076	0.001	0.38	0.024	0.001	10	43	388	0.11	13.25	0.89	0.057	1.69	469.2	4.0
VM19-14	24	24c	mantle	0.583	0.008	0.075	0.001	0.31	0.023	0.001	7	31	299	0.10	13.30	0.84	0.056	1.56	467.4	3.8
VM19-14	36	36b	mantle	0.586	0.009	0.075	0.001	0.46	0.023	0.001	8	37	569	0.06	13.34	1.12	0.057	1.66	465.9	5.1
VM19-14	35	35a	mantle	0.674	0.030	0.074	0.002	0.11	0.040	0.003	13	36	399	0.09	13.50	3.24	0.066	4.07	461.0	14.0
smaller fraction:																				
VM19-14	56	56a	core	0.682	0.019	0.085	0.001	0.26	0.026	0.001	4	15	56	0.28	11.82	1.54	0.059	2.90	523.4	7.9
VM19-14	64	64a	mantle	0.605	0.012	0.077	0.001	0.35	0.026	0.001	5	19	188	0.10	13.00	1.30	0.057	2.27	477.5	6.0
VM19-14	56	56b	mantle	0.594	0.012	0.077	0.002	0.63	0.024	0.001	13	63	1086	0.06	13.07	2.09	0.057	1.94	475.2	9.5
VM19-14	64	64b	mantle	0.604	0.013	0.076	0.001	0.37	0.023	0.001	12	52	181	0.29	13.09	1.31	0.057	2.10	474.5	6.1
VM19-14	70	70a	mantle	0.598	0.011	0.076	0.001	0.44	0.025	0.001	10	42	663	0.06	13.12	1.44	0.057	1.76	473.4	6.7
VM19-14	67	67b	mantle	0.604	0.012	0.076	0.001	0.46	0.023	0.001	9	41	316	0.13	13.13	1.30	0.057	1.92	473.1	5.9
VM19-14	70	70b	mantle	0.596	0.011	0.076	0.001	0.45	0.023	0.001	13	61	321	0.19	13.13	1.31	0.057	1.94	473.1	6.2
VM19-14	67	67a	rim	0.611	0.008	0.041	0.001	0.81	0.223	0.006	191	91	3250	0.03	24.38	2.36	0.109	1.75	259.0	6.0
AM19-25	78	78a	core	22.060	0.400	0.592	0.010	0.71	0.164	0.004	266	178	344	0.52	1.69	1.62	0.269	1.60	3002.0	37.0
AM19-25	65	65b	mantle	4.514	0.079	0.296	0.004	0.60	0.083	0.002	86	115	160	0.72	3.38	1.49	0.110	1.54	1669.0	22.0
AM19-25	65	65a	mantle	2.953	0.042	0.208	0.003	0.71	0.077	0.002	94	127	388	0.33	4.80	1.25	0.103	1.37	1219.0	14.0
AM19-25	97	97a	core	0.778	0.013	0.094	0.001	0.41	0.028	0.001	53	207	320	0.65	10.66	1.17	0.060	1.66	578.1	6.2
AM19-25	78	78b	mantle	0.730	0.015	0.086	0.001	0.72	0.026	0.001	13	59	1105	0.05	11.67	1.52	0.062	1.61	529.7	7.5
AM19-25	97	97b	mantle	0.711	0.011	0.080	0.001	0.24	0.073	0.005	41	65	1517	0.04	12.44	1.37	0.064	1.87	498.3	6.4
AM19-25	69	69	mantle	0.607	0.009	0.077	0.001	0.48	0.023	0.001	9	44	430	0.10	12.94	0.97	0.057	1.52	479.9	4.5
AM19-25	66	66a	mantle	0.614	0.012	0.077	0.001	0.59	0.023	0.001	7	34	510	0.07	12.95	1.68	0.058	1.91	479.3	8.0
AM19-25	81	81	mantle	0.607	0.009	0.077	0.001	0.44	0.024	0.001	10	45	429	0.10	13.00	1.04	0.057	1.63	477.8	4.8
AM19-25	72	72	mantle	0.598	0.008	0.077	0.001	0.49	0.024	0.001	9	42	524	0.08	13.05	0.94	0.056	1.44	475.8	4.3
AM19-25	66	66b	mantle	0.604	0.009	0.077	0.001	0.46	0.024	0.001	9	38	521	0.07	13.05	1.11	0.057	1.55	475.7	5.1
AM19-25	64	64	mantle	0.596	0.013	0.076	0.001	0.64	0.023	0.001	8	37	597	0.06	13.11	1.83	0.057	1.94	474.0	8.2
AM19-25	70	70	mantle	0.595	0.008	0.076	0.001	0.49	0.022	0.000	72	346	548	0.63	13.15	0.91	0.057	1.41	472.5	4.2
AM19-25	83	83	mantle	0.600	0.009	0.076	0.001	0.23	0.024	0.001	6	27	336	0.08	13.19	1.00	0.057	1.75	471.0	4.6
AM19-25	96	96	mantle	0.590	0.008	0.076	0.001	0.49	0.023	0.001	10	48	651	0.07	13.25	0.98	0.056	1.44	469.1	4.4
AM19-25	68	68a	mantle	0.590	0.008	0.075	0.001	0.42	0.023	0.001	11	54	357	0.15	13.25	0.97	0.057	1.61	469.1	4.4
AM19-25	85	85	mantle	0.591	0.014	0.075	0.002	0.67	0.025	0.002	10	45	736	0.06	13.26	2.12	0.057	2.10	468.2	9.8
AM19-25	71	71	mantle	0.590	0.008	0.075	0.001	0.53	0.024	0.001	14	65	841	0.08	13.29	1.00	0.057	1.39	467.6	4.5
AM19-25	68	68b	mantle	0.706	0.018	0.065	0.002	0.51	0.056	0.002	35	70	595	0.12	15.43	2.16	0.079	2.53	404.6	8.4

Table 5: Zircon age data.

To answer the question if the investigated rock is whether a meta-granite or -rhyolite the following aspect is important: The short prismatic habit of the investigated zircons indicates a plutonic and not volcanic origin of the orthogneiss. Long prismatic zircons are characteristic for fast growth in a fast cooling medium, i.e. volcano in the main sense, whereas short prismatic zircons are more characteristic for a slow cooling medium (Corfu et al., 2003). Hence, a plutonic origin as sills or laccoliths is most likely.

We suggest to discriminate between two types of the Laimbach Orthogneiss, based on their position within the Ostrong N.S.: Type 1 for the central and western parts and Type 2 for the easternmost parts near the tectonic boundary to the Drosendorf N.S.. The differences between these two types range from the macroscopic appearance over the mineralogy to the geochemistry (Chapt. 4.1–4.3). The fact, that incompatible elements such as REE and Zr are lower in Type 2 compared to Type 1, suggests that Type 2 is less differentiated than Type 1. Furthermore, Type 2 shows the highest K/Rb and U/Th ratios from all samples. A distinctive feature is the appearance of quartz-sillimanite-aggregates in both Type 1 and Type 2. Conversely, these aggregates are absent in sample VM19-19, which represents an orthogneiss from the "Aplite, pegmatite, granite gneiss" (Fig. 2) occurrences in the Ostrong N.S. and which we don't rate among the Laimbach Orthogneiss Lithodem. To discuss the geochronological connection between Type 1 and 2 a further U-Pb zircon age determination for Type 2 in the future would be necessary. A future search for Topaz in heavy mineral concentrates of Type 2 would also be interesting. We interpret the differences between Type 1 and 2 as results of a slightly different genesis during the Variscan Orogeny.

Sample VM19-19 as an orthogneiss representative for the occurrences of "Aplite, pegmatite, granite gneiss" (Fig. 2) in the Ostrong N.S. shows too many differences to the Type 1 and 2 samples to be seen as part of the Laimbach Orthogneiss Lithodem. One of the geochemical differences is the slightly higher enrichment in incompatible elements such as REE and Zr in VM19-19 (Chapt. 4.2), which indicates that sample VM19-19 is slightly more differentiated than the Laimbach Orthogneiss Lithodem. Furthermore, VM19-19 bears no sillimanite-quartz-aggregates, which are characteristic for the Laimbach Orthogneiss Lithodem and is thus the most significant difference.

5.2 Protolith and genesis of the Laimbach Orthogneiss

The Th/U ratios of some zircons are lower than the typical values for magmatic or anatectic zircons from felsic magmas of about 0.3–1.2 (Heaman et al., 1990; Schaltegger et al., 1999; Vavra et al., 1999). For low Th/U ratios of < 0.1 and even < 0.05, metamorphic zircon formation is assumed (Vavra et al., 1996; Schaltegger et al., 1999; Rub-

atto, 2002). In the present case, however, a metamorphic origin can be excluded, since oscillatory zoning is a likely sign of igneous origin (Pidgeon, 1992; Corfu et al., 2003).

The concordia ages 475.3 ± 1.0 Ma, 474.8 ± 2.9 Ma and 473.5 ± 1.5 Ma define the magmatic formation age of the zircons. These measurement points were placed in the areas of oscillatory zoning whose origin is related to magmatic or anatectic zircon growth (Pidgeon, 1992). The dark, discordant overgrowths possibly represent metamorphic regrowth during the Variscan orogeny.

The zircon cores measured represent inherited cores, since they are older than their mantle and rim regions. These cores can be divided into three age groups: (A) Late Cadomian, with three zircon cores preserving dates from 523.4 ± 7.9 Ma to 578.1 ± 6.2 Ma. (B) Early Cadomian, with one core at 628.3 ± 6.4 Ma. (C) Archean, with one 3002.0 ± 37.0 Ma old core being the oldest measured in this work. The two core ages (1219.0 ± 14.0 Ma and 1669.0 ± 22.0 Ma) of zircon No. 65 are rather to be taken as exceptions or as inherited zircon cores, typical for S-type granitoids, like the age groups A–C.

5.3 Comparison with other metagranitoids and orthogneisses of the Moldanubian Nappes

For a consideration of the Laimbach Orthogneiss in a bigger tectonic framework, the geochemical and geochronological results are compared with those of other metagranitoids and orthogneisses of the Moldanubian Nappes, assuming that the metamorphic overprinting was isochemical. We compare the Laimbach Orthogneiss with rocks investigated in different geological units: A) The Dobra Gneiss (ca. 1.4 Ga, 600 Ma; Lindner et al., 2020) and Spitz Gneiss (ca. 610 Ma; Lindner and Finger, 2018) from the Drosendorf N.S.. B) The Gföhl Gneiss (between 460 and 500 Ma; Friedl et al., 2004; René and Finger, 2016) and the Moldanubian Granulite (between 430 and 490 Ma; Kröner et al., 2000; Janoušek et al., 2004; Friedl et al., 2004, 2011) from the Gföhl N.S.. C) The Blaník Gneiss from the Ostrong N.S. in the Czech Republic (ca. 510 Ma; Vrána and Kröner, 1995; René and Finger, 2016), leucocratic plagioclase-orthogneiss occurrences in a similar unit of the Ostrong N.S. in the Bavarian Forest (ca. 485 Ma; Group IV from Teipel (2003)) and the Leptinitic Gneiss from the Moldanubian in Bavaria (Precambrian age assumed) sensu Richter and Stettner (1983). The most meaningful and representative results of the geochemical comparison are shown in Figure 7.

The Gföhl Gneiss, the Moldanubian Granulite and the Blaník Gneiss show the greatest similarities with the Laimbach Orthogneiss, whereas the Blaník Gneiss shows the least similarities. The Blaník Gneiss has, compared to the Laimbach Orthogneiss, the Gföhl Gneiss and the Moldanubian Granulite, for example a lower content of Zr and U is strongly elevated. The low K/Rb ratio and high SiO_2 content suggest that the Laimbach Orthogneiss is the most differentiated rock. It shows the least similarity to the Dobra and Spitz Gneiss (Fig. 7). The Dobra and
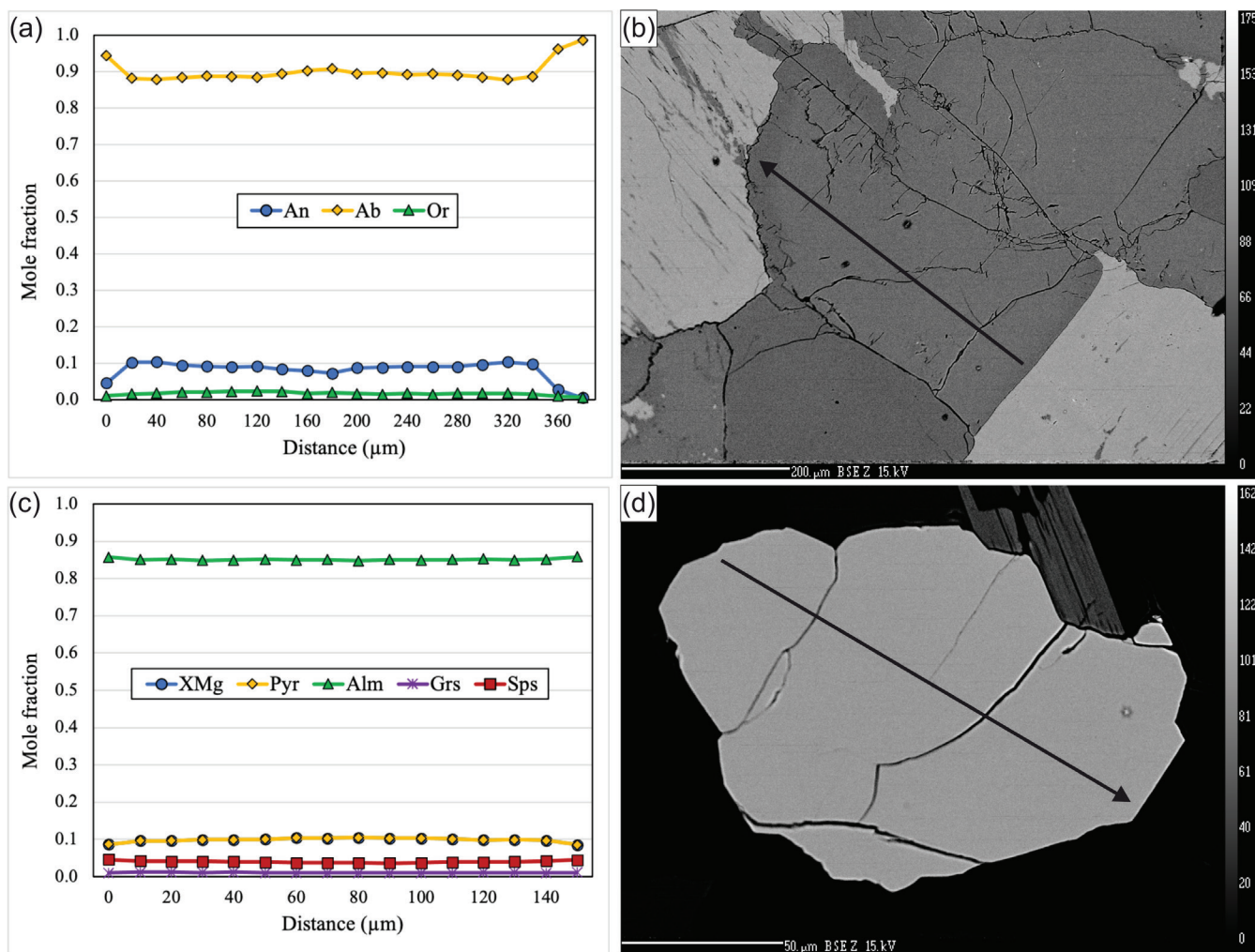
Figure 8: EPMA major element concentration profiles showing endmember composition for (a) plagioclase in sample VM19-14 and (c) garnet in sample AM19-23. (b) Backscattered electrons (BSE) image of plagioclase from (a) (by EPMA) and (d) BSE image of (c) (by EPMA).
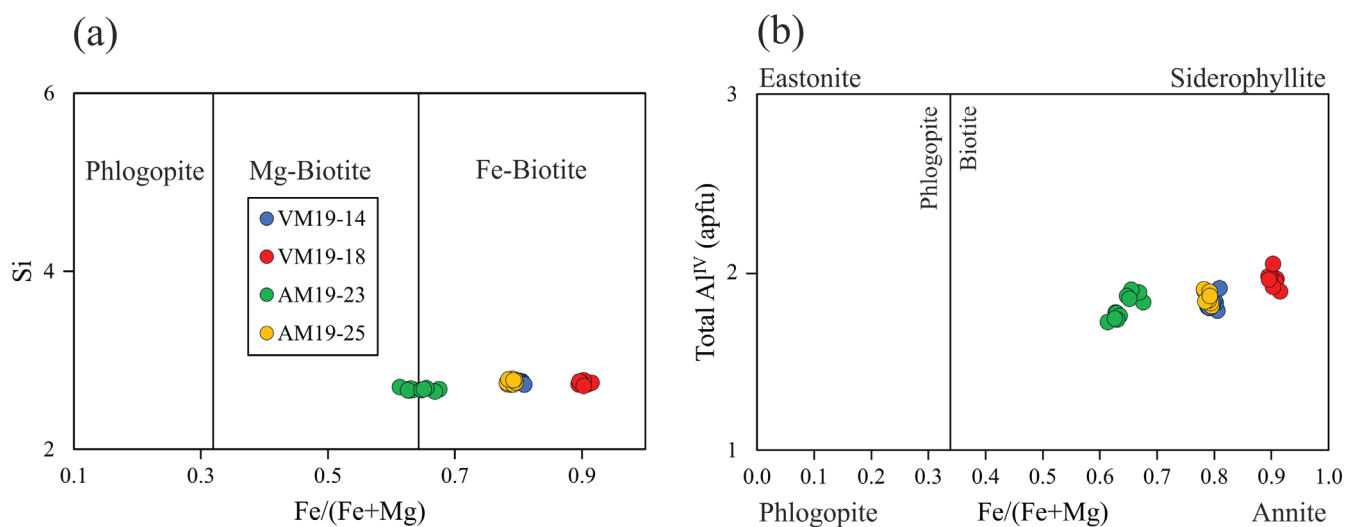

Figure 9: Biotite chemistry classification diagrams after Deer et al. (2001). apfu = atoms per formula unit.
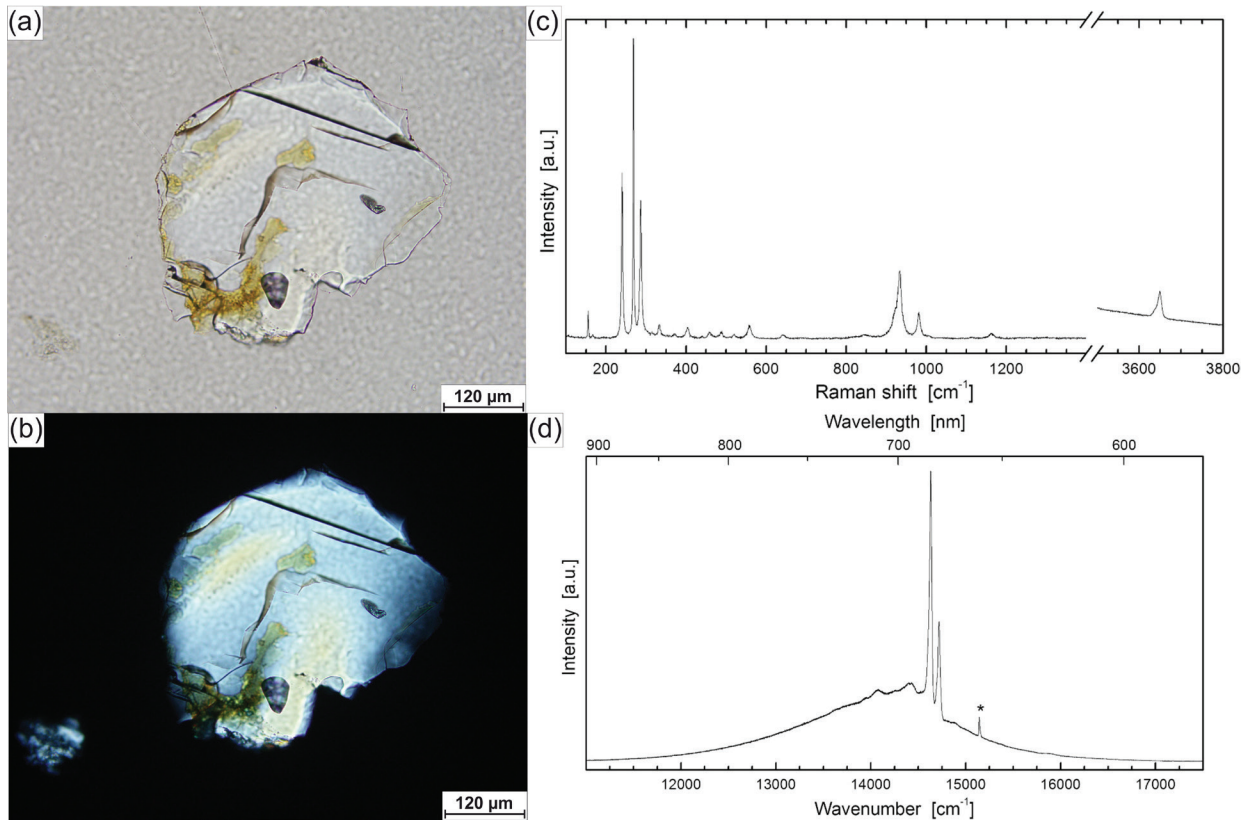
Figure 10: Photomicrographs of topaz from sample VM19-14 under (a) plane- and (b) cross-polarized light. (c) Raman spectrum of topaz from sample VM19-14, in the "lattice" and hydroxyl-stretching regions. The latter is affected by background due to laser-induced PL in the near-infrared spectral range. (d) Emission spectrum of topaz from sample VM19-14. The asterisk marks the O–H stretching Raman band excited by the 532 nm laser.
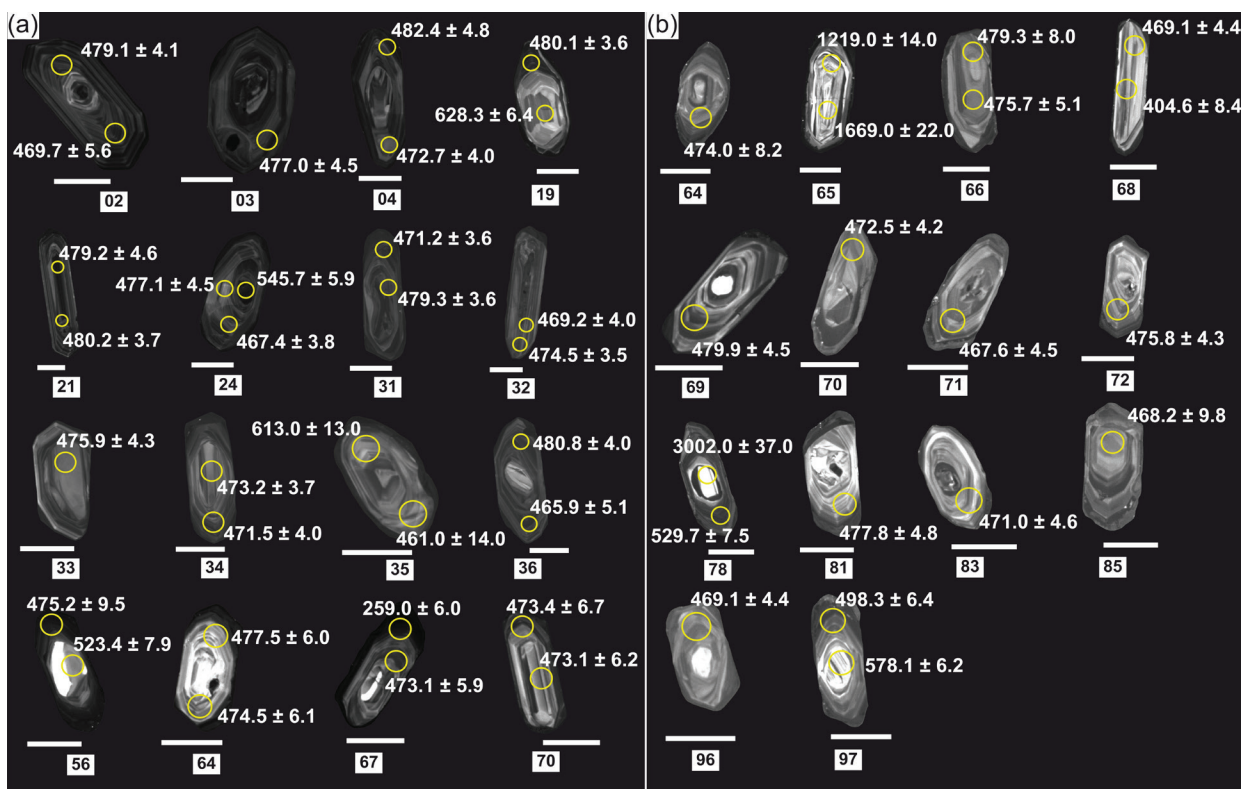
Figure 11: Cathodoluminescence images of the dated zircons with the measurement points and the respective $^{206}Pb/^{238}U$ ages and 2 SE uncertainty estimates. (a) Analyses of sample VM19-14. Here, zircons nos. 56, 64, 67 and 70 belong to the smaller fraction, the others to the larger one. (b) Analyses of sample AM19-25. Scale bar is 50 µm.

Figure 12: (a) Tera-Wasserburg concordia diagram of the larger zircon fraction of sample VM19-14. The ellipses define the 475.3 ± 1.0 Ma concordia age group. (b) Tera-Wasserburg concordia diagram of the smaller zircon fraction of sample VM19-14. The ellipses define the 474.8 ± 2.9 Ma concordia age group. (c) Tera-Wasserburg concordia diagram of the zircons of sample AM19-25. The ellipses define the 473.5 ± 1.5 Ma concordia age group.

Spitz Gneiss have a much higher Sr content, typical for I-type granites, whereas the Laimbach Orthogneiss has a low Sr content, more typical for S-type granites. In the other discriminations they also show the strongest discrepancy to the Laimbach Orthogneiss. Due to its high F content, the Leptinitic Gneiss from the Bavarian Forest according to Richter and Stettner (1983) was used for comparison, whose F content is even higher than in the Laimbach Orthogneiss. Other elements, however, do not show greater similarities.

Of special interest is an occurrence of metagranites in a similar geotectonic position in the Bavarian Forest (Germany; Teipel, 2003), and with a similar Lower Ordovician age than the Laimbach Orthogneiss. These leucocratic plagioclase-orthogneisses (Group IV after Teipel, 2003) are located in a similar unit of the Ostrong N.S., close to rocks of the Drosendorf N.S.. Their origin as Gondwana derived crustal elements with a genesis along a continental margin is a possible interpretation also for the Laimbach Orthogneiss. However, whole-rock compositions do not show strong similarities.

Summarizing, the comparison with other metagranitoids and orthogneisses of the Bohemian Massif shows that there is a connection to rocks of the Gföhl N.S., with a strong geochemical similarity to the Gföhl Gneiss and the Moldanubian Granulite. Compared to these two rocks, the Laimbach Orthogneiss is more differentiated. Furthermore, Riedel (1930) and Fuchs et al. (1990) already mentioned similarities between the Laimbach and Gföhl Gneisses. It seems possible that the Gföhl Gneiss and the Moldanubian Granulite have a common magmatic source with the Laimbach Orthogneiss and have gone through a similar further evolutionary history, differing only in the higher degree of fractionation of the Laimbach Orthogneiss. The geochemical composition of the Blaník Gneiss differs too much from that of the Laimbach Orthogneiss to support a closer connection of the two at this point. At least the Laimbach Orthogneiss is not related to the Spitz and Dobra Gneiss of the Drosendorf N.S.. In addition, these findings support the previously mentioned concept that the rocks of the Drosendorf N.S. are of a different plate tectonic origin [Bruno-Vistulian (Avalonia)] than the Gföhl and Ostrong N.S. [Moldanubian (Armorica/Galatia)] (Finger and Schubert, 2015; Lindner et al., 2021). Zircon U-Pb ages of the Laimbach Orthogneiss (concordia ages 475.3 ± 1.0 Ma, 474.8 ± 2.9 Ma and 473.5 ± 1.5 Ma) correspond with the protolith ages of the Gföhl Gneiss (between 460 and 500 Ma; Friedl et al., 2004) and

those of the Moldanubian Granulite respectively (approximately between 430 and 490 Ma; Kröner et al., 2000; Friedl et al., 2004, 2011). The Blaník Gneiss definitely has an older zircon age of ca. 508 ± 7 Ma (Vrána and Kröner, 1995).

6. Conclusions

Finally, we draw the following conclusions about the Laimbach Orthogneiss:

- Topaz found in the Laimbach Orthogneiss characterizes the latter as the source for the trace content of topaz in channels draining the eastern slope of the Ostrong mountain, which was prospected by Göd (1988). Raman data characterize the topaz in the Laimbach Orthogneiss as F-rich.
- The geochemical characteristics of the orthogneiss indicate a classification as S-type granite or -rhyolite with a high degree of differentiation. The short prismatic habit of the zircons indicates a plutonic and not volcanic origin of the protolith. Therefore, an origin as granitic intrusion is proposed.
- Based on petrography and geochemistry, we distinguished two types: Type 1 includes samples taken from the more westerly occurrences and showing weaker tectonic overprinting than Type 2, showing weak to well-developed foliation, as well as local folding. Type 2 includes samples taken near the tectonic boundary of the Ostrong- to the Drosendorf Nappe System. They show stronger shear deformation with pronounced mylonitic foliation and stretching lineation. We interpret the differences between Type 1 and 2 as results of a slightly different genesis during the Variscan Orogeny.
- Mineral chemistry data show zoned plagioclase with an albite component of about 87–99 mol%, increasing towards the grain margin. Almandine-dominated garnet occurs in Type 2 samples, which shows no zoning and is single-phased. The rock carries sillimanite throughout and also relict kyanite in Type 2 samples.
- Igneous zircon growth ages are 475.3 ± 1.0 Ma, 474.8 ± 2.9 Ma and 473.5 ± 1.5 Ma.
- The Laimbach Orthogneiss is considered as a more fractionated equivalent of the Gföhl Gneiss, based on geochemical and geochronological data.
- Following the North American Stratigraphic Code (NACSN, 2005), we suggest to classify the Laimbach Orthogneiss in the rank of a lithodeme.

References

Anders, E., Grevesse, N., 1989. Abundances of the elements: Meteoritic and solar. Geochimica et Cosmochimica acta, 53, 197–214.

Beny, J.M., Piriou, B., 1987. Vibrational spectra of single-crystal topaz. Physics and Chemistry of Minerals, 15, 148–154.

Brandmayr, M., Loizenbauer, J., Wallbrecher, E., 1999. Contrasting P-T conditions during conjugate shear zone development in the Southern Bohemian Massif, Austria. Mitteilungen der Österreichischen Geologischen Gesellschaft, 90, 11–29.

Büttner, S.H., 2007. Late Variscan stress-field rotation initiating escape tectonics in the south-western Bohemian Massif: A far field response to late-orogenic extension. Journal of Geosciences, 52, 29–43.

Carswell, D.A., 1991. Variscan high P-T metamorphism and uplift history in the Moldanubian Zone of the Bohemian Massif in Lower Austria. European Journal of Mineralogy, 3, 323–342.

Cháb, J., Stráník, Z., Eliáš, M., 2007. Geologická mapa České republiky 1:500 000. Česká geologická služba, Praha.

Corfu, F., Hanchar, J.M., Hoskin, P.W.O., Kinny, P., 2003. Atlas of zircon textures. Reviews in Mineralogy and Geochemistry, 53/1, 469–500.

Deer, W.A., Howie, R.A., Zussman, J., 2001. An introduction to the rock-forming minerals. Second Edition. Longman, London, 1–972.

Finger, F., Schubert, G., 2015. Die Böhmische Masse in Österreich. Was gibt es Neues. Abhandlungen der Geologischen Bundesanstalt, 64, 167–179.

Franke, W., 2000. The mid-European segment of the Variscides: tectonostratigraphic units, terrane boundaries and plate tectonic evolution. Geological Society of London, Special Publications, 179, 35–61.

Friedl, G., Cooke, R.A., Finger, F., McNaughton, N.J., Fletcher, I.R., 2011. Timing of Variscan HP-HT metamorphism in the Moldanubian Zone of the Bohemian Massif: U-Pb SHRIMP dating on multiply zoned zircons from a granulite from the Dunkelsteiner Wald Massif, Lower Austria. Mineralogy and Petrology, 102, 63–75.

Friedl, G., Finger, F., Paquette, J.L., von Quadt, A., McNaughton, N.J., Fletcher, I.R., 2004. Pre-Variscan geological events in the Austrian part of the Bohemian Massif deduced from U–Pb zircon ages. International Journal of Earth Sciences, 93, 802–823.

Fuchs, G., Fuchs, W., 1986. Geologische Karte der Republik Österreich, 1:50000, Blatt 36 Ottenschlag. Geologische Bundesanstalt, Wien.

Fuchs, G., Roetzel, R., Heinz, H., 1990. Erläuterungen zu Blatt 36 Ottenschlag. Geologische Bundesanstalt, Wien.

Fuchs, G., 2005. Der geologische Bau der Böhmischen Masse im Bereich des Strudengaus (Niederösterreich). Jahrbuch der Geologischen Bundesanstalt, 145, 283–291.

Göd, R., 1988. Zusammenfassende Übersicht über ausgeführte Erzprospektionsvorhaben, dabei eingesetzte Methoden sowie Hoffnungsgebiete im Kristallin der Böhmischen Masse. Projekt OC 6a/87, Geologische Bundesanstalt, Wien.

Göd, R., 1989. A contribution to the Mineral Potential of the Southern Bohemian Massif, Austria. Arch. Lagerst.-forsch. Ostalpen, Bd. 11, 147–153, Geologische Bundesanstalt, Wien.

Graf, T., 2017. Petrographische Beschreibung leukokraten, Sillimanit-

führenden Orthogneisen und deren Schwermineralspektrum in der Monotonen Serie, Ostrong, Böhmische Masse. Unveröffentl. Bachelorarbeit, Universität Wien.

Heaman, L.M., Bowins, R., Crocket, J., 1990. The chemical composition of igneous zircon suites: implications for geochemical tracer studies. Geochimica et Cosmochimica Acta, 54, 1597–1607.

Högelsberger, H., 1989. Die Marmore und Kalksilikatgesteine der Bunten Serie – Petrologische Untersuchungen und geologische Konsequenzen. Jahrbuch der Geologischen Bundesanstalt, 132, 213–230.

Janoušek, V., Finger, F., Roberts, M., Frýda, J., Pin, C., Dolejš, D., 2004. Deciphering the petrogenesis of deeply buried granites: whole-rock geochemical constraints on the origin of largely undepleted felsic granulites from the Moldanubian Zone of the Bohemian Massif. Earth and Environmental Science Transactions of The Royal Society of Edinburgh, 95, 141–159.

Kossmat, F., 1927. Gliederung des varistischen Gebirgsbaues. Abhandlungen des Sächsischen Geologischen Landesamtes, 1, 1–39.

Krenmayr, H.G., Schnabel, W., Bryda, G., Egger, H., Finger, F., Linner, M., Mandl, G.W., Nowotny, A., Pestal, G., Reitner, J.M., Roetzel, R., Rupp, C., Schuster, R., Van Husen, D., 2006. Geologische Karte von Oberösterreich 1:200 000. Geologische Bundesanstalt, Wien.

Kroner, U., Romer, R.L., 2013. Two plates - Many subduction zones: The Variscan orogeny reconsidered. Gondwana Research, 24, 298–329.

Kröner, A., O'Brien, P.J., Nemchin, A.A., Pidgeon, R.T., 2000. Zircon ages for high pressure granulites from South Bohemia, Czech Republic, and their connection to Carboniferous high temperature processes. Contributions to Mineralogy and Petrology, 138, 127–142.

Lindner, M., Finger, F., 2018. Geochemical characteristics of the Late Proterozoic Spitz granodiorite gneiss in the Drosendorf Unit (Southern Bohemian Massif, Austria) and implications for regional tectonic interpretations. Journal of Geosciences, 63, 345–362.

Lindner, M., Dörr, W., Reither, D., Finger, F., 2021. The Dobra Gneiss and the Drosendorf Unit in the south-eastern Bohemian Massif, Austria: West-Amazonian crust in the heart of Europe. Geological Society, London, Special Publications, 503.

Linner, M., 1996. Metamorphism and partial melting of paragneisses of the Monotonous Group, SE Moldanubicum (Austria). Mineralogy and Petrology, 58, 215–234.

Linner, M., 2013. Metamorphoseentwicklung und Deckenbau des Moldanubikums mit Fokus auf den Raum Melk – Dunkelsteinerwald. In: Gebhardt, H. (eds.) Tagungsband zur Arbeitstagung 2013 der Geologischen Bundesanstalt. Geologie der Kartenblätter 55 Ober-Grafendorf und 56 St. Pölten, Wien, 43–56.

Middlemost, E.A., 1994. Naming materials in the magma/igneous rock system. Earth-Science Reviews, 37, 215–224.

Nance, R.D., Gutiérrez-Alonso, G., Keppie, J.D., Linnemann, U., Murphy, J.B., Quesada, C., Strachan, R.A., Woodcock, N.H., 2010. Evolution of the Rheic Ocean. Gondwana Research, 17/2–3, 194–222.

NACSN (North American Commission on Stratigraphic Nomenclature), 2005. North American Stratigraphic Code. - AAPG (Advancing the World of Petroleum Geosciences) Bulletin, 89/11, 1547–1591, Tulsa.

O'Bannon, E.F., Williams, Q., 2019. A Cr^{3+} luminescence study of natural topaz $Al_2SiO_4(F,OH)_2$ up to 60 GPa. American Mineralogist, 104, 1656–1662.

Petrakakis, K., 1997. Evolution of Moldanubian rocks in Austria: review and synthesis. Journal of Metamorphic Geology, 15, 203–222.

Pidgeon, R.T., 1992. Recrystallisation of oscillatory zoned zircon: some geochronological and petrological implications. Contributions to Mineralogy and Petrology, 110, 463–472.

Pinheiro, M.V.B., Fantini, C., Krambrock, K., Persiano, A.I.C., Dantas, M.S.S., Pimenta, M.A., 2002. OH/F substitution in topaz studied by Raman spectroscopy. Physical Review B, 65, 1–6.

Racek, M., Štípská, P., Pitra, P., Schulmann, K., Lexa, O., 2006. Metamorphic record of burial and exhumation of orogenic lower and middle crust: a new tectonothermal model for the Drosendorf window (Bohemian Massif, Austria). Mineralogy and Petrology, 86, 221–251.

René, M., Finger, F., 2016. The Blaník Gneiss in the southern Bohemian Massif (Czech Republic): a rare rock composition among the early palaeozoic granites of Variscan Central Europe. Mineralogy and Petrology, 110, 503–514.

Richter, P., Stettner, G., 1983. Das Präkambrium am Nordrand der Moldanubischen Region im Raum Tirschenreuth-Mähring (NE-Bayern) und dessen metallogenetische Aspekte: Lithostratigraphische, petrographische und geochemische Untersuchungen. Geol. Jb., D61, 23–91.

Riedel, J., 1930. Der geologische Bau des Gebietes zwischen dem Ostrong und der Granitgrenze im niederösterreichischen Waldviertel. Zeitschrift für Kristallographie, Mineralogie und Petrographie, 40, 235–293.

Rudnick, R.L., Gao, S., 2005. Composition of the continental crust. In: Rudnick, R.L. (ed.), The crust. Elsevier Science, Amsterdam, 3, 1–64.

Rubatto, D., 2002. Zircon trace element geochemistry: partitioning with garnet and the link between U–Pb ages and metamorphism. Chemical Geology, 184, 123–138.

Schaltegger, U., Fanning, C.M., Günther, D., Maurin, J.C., Schulmann, K., Gebauer, D., 1999. Growth, annealing and recrystallization of zircon and preservation of monazite in high-grade metamorphism: conventional and in-situ U-Pb isotope, cathodoluminescence and microchemical evidence. Contributions to Mineralogy and Petrology, 134, 186–201.

Schantl, P., Hauzenberger, C., Finger, F., Müller, T., Linner, M., 2019. New evidence for the prograde and retrograde PT-path of high-pressure granulites, Moldanubian Zone, Lower Austria, by Zr-in-rutile thermometry and garnet diffusion modelling. Lithos, 342, 420–439.

Schnabel, W., Bryda, G., Egger, H., Fuchs, G., Krenmayr, H.G., Mandl, G.W., Matura, A., Nowotny, A., Roetzel, R., Scharbert, S., Wessely, G., 2002. Geologische Karte von Niederösterreich 1:200 000. Geologische Bundesanstalt, Wien.

Schulmann, K., Kröner, A., Hegner, E., Wendt, I., Konopásek, J., Lexa, O., Štípská, P., 2005. Chronological constraints on the pre-orogenic history, burial and exhumation of deep-seated rocks along the eastern margin of the Variscan orogen, Bohemian Massif, Czech Republic. American Journal of Science, 305, 407–448.

Shand, S.J., 1943. Eruptive Rocks. Their Genesis, Composition, Classification, and Their Relation to Ore-Deposits with a Chapter on Meteorite. John Wiley & Sons, New York, 444 pp.

Soejono, I., Machek, M., Sláma, J., Janoušek, V., Kohút, M., 2020. Cambro-Ordovician anatexis and magmatic recycling at the thinned Gondwana margin: new constraints from the Kouřim Unit, Bohemian Massif. Journal of the Geological Society, 177, 325–341.

Stampfli, G.M., Hochard, C., Vérard, C., Wilhem, C., Raumer, J.v., 2013. The formation of Pangea. Tectonophysics, 593, 1–19.

Suess, F.E., 1911. Die Moravischen Fenster und ihre Beziehung zum Grundgebirge des Hohen Gesenkes. Denkschriften der Kaiserlichen Akademie der Wissenschaften Mathematisch-naturwissenschaftliche Klasse, 88, 541–631.

Suess, F.E., 1926. Intrusionstektonik und Wandertektonik im Variszischen Grundgebirge. Borntraeger, Berlin, 268 pp.

Tarashchan, A.N., Taran, M.N., Rager, H., Iwanuch, W., 2006. Luminescence spectroscopic study of Cr^{3+} in Brazilian topazes from Ouro Preto. Physics and Chemistry of Minerals, 32, 679–690.

Taylor, S.R., McLennan, S.M., 1995. The geochemical evolution of the continental crust. Reviews of Geophysics, 33, 241–265.

Teipel, U., 2003. Obervendischer und Unterordovizischer Magmatismus im Bayerischen Wald – Geochronologische (SHRIMP), geochemische und isotopengeochemische Untersuchungen an Metamagmatiten aus dem Westteil des Böhmischen Massivs. Münchner Geologische Hefte, 98 pp.

Tollmann, A., 1982. Großräumiger variszischer Deckenbau im Moldanubikum und neue Gedanken zum Variszikum Europas. Geotektonische Forschungen, 64, 1–91.

Vavra, G., Gebauer, D., Schmid, R., Compston, W., 1996. Multiple zircon growth and recrystallization during polyphase Late Carboniferous to Triassic metamorphism in granulites of the Ivrea Zone (Southern Alps): an ion microprobe (SHRIMP) study. Contributions to Mineralogy and Petrology, 122, 337–358.

Vavra, G., Schmid, R., Gebauer, D., 1999. Internal morphology, habit and U-Th-Pb microanalysis of amphibolite-to-granulite facies zircons: geochronology of the Ivrea Zone (Southern Alps). Contributions to Mineralogy and Petrology, 134, 380–404.

Vrána, S., Kröner, A., 1995. Pb-Pb zircon ages for tourmaline alkali-feldspar orthogneiss from Hluboká nad Vltavou in southern Bohemia. Journal of the Czech Geological Society, 40, 127–131.

Wallbrecher, V.E., Brandmayer, M., Loizenbauer, J., Handler, R., Dallmeyer, R.D., 1996. Konjugierte Scherzonen in der südlichen Böhmischen Masse: variszische und alpidische kinematische Entwicklungen. Exkursionsunterlagen für die Wandertagung 1996: Ein Querschnitt durch die Geologie Oberösterreichs, 12–28.

ZOBODAT - www.zobodat.at